Review Article

Jia Xue Zhai, Lin Xie*, and Shafidah Shafian*

Advancements in perovskite/CIGS tandem solar cells: Material synergies, device configurations, and economic viability for sustainable energy

https://doi.org/10.1515/ntrev-2025-0196
received February 6, 2025; accepted June 22, 2025

Abstract: The growing demand for renewable energy is driving innovations in solar technology for both outdoor and indoor applications. However, higher efficiency, improved stability, and cost-effectiveness are the highest priorities for the commercialization of solar cells. Recently, tandem solar cells (T-SCs) have emerged as a promising solution to surpass the efficiency limits of traditional single-junction cells. By integrating materials like perovskite and copper–indium–gallium–selenide (CIGS), T-SCs capture a broader spectrum of sunlight, improving power conversion efficiency. Perovskite's wide bandgap (~1.6 eV) absorbs high-energy photons, while CIGS's narrower bandgap (~1.1 eV) optimizes lower-energy photon absorption. This review examines recent developments in perovskite/CIGS T-SCs, highlighting the complementary properties of these materials and their impact on photocurrent generation. It also compares two-terminal (2-T) and four-terminal (4-T) configurations, achieving efficiencies of 24.6 and 30.1%, respectively. Additionally, the economic potential of perovskite/CIGS T-SCs is explored, focusing on their role in reducing energy costs and enhancing sustainability. Key challenges and future directions are also discussed to advance renewable energy systems.

Keywords: perovskite solar cell, CIGS solar cell, tandem solar cell, efficiency, economic viability

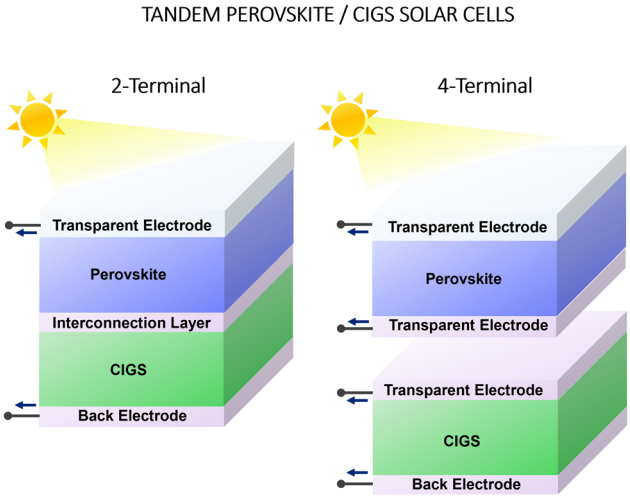

Graphical abstract: The growing demand for renewable energy drives advancements in solar technologies, with tandem solar cells (T-SCs) gaining attention for exceeding the efficiency limits of traditional cells. T-SCs combine perovskite and copper–indium–gallium–selenide materials to enhance power conversion efficiency by capturing a broader solar spectrum. This review explores recent developments, design considerations, efficiencies, and economic potential.

1 Introduction

The growing demand for renewable energy sources has accelerated research in photovoltaic (PV) technologies, with solar energy emerging as a key player in the transition toward sustainable energy systems [1]. Among the various PV technologies, tandem solar cells (T-SCs) have gained significant attention due to their potential to exceed the efficiency limits of conventional single-junction solar cells [2]. T-SCs combine two or more absorbing materials, effectively utilizing a broader range of the solar spectrum and thereby enhancing power conversion efficiencies (PCEs). Several perovskite-based tandem architectures have been explored, including all-perovskite [3], perovskite/silicon [4], perovskite/thin-film (*e.g.*, perovskite/copper–indium–gallium selenide (CIGS) [5], perovskite/copper–indium–selenide (CIS) [6], and perovskite/cadmium

* **Corresponding author: Lin Xie,** School of Materials and Energy, Yunnan University, Kunming, 650091, China; International Joint Research Center for Optoelectronic and Energy Materials, Yunnan University, Kunming, 650091, China, e-mail: l.xie@ynu.edu.cn
* **Corresponding author: Shafidah Shafian,** Solar Energy Research Institute, Universiti Kebangsaan Malaysia, Bangi, Selangor, 43600, Malaysia, e-mail: norshafidah@ukm.edu.my
Jia Xue Zhai: School of Materials and Energy, Yunnan University, Kunming, 650091, China; International Joint Research Center for Optoelectronic and Energy Materials, Yunnan University, Kunming, 650091, China

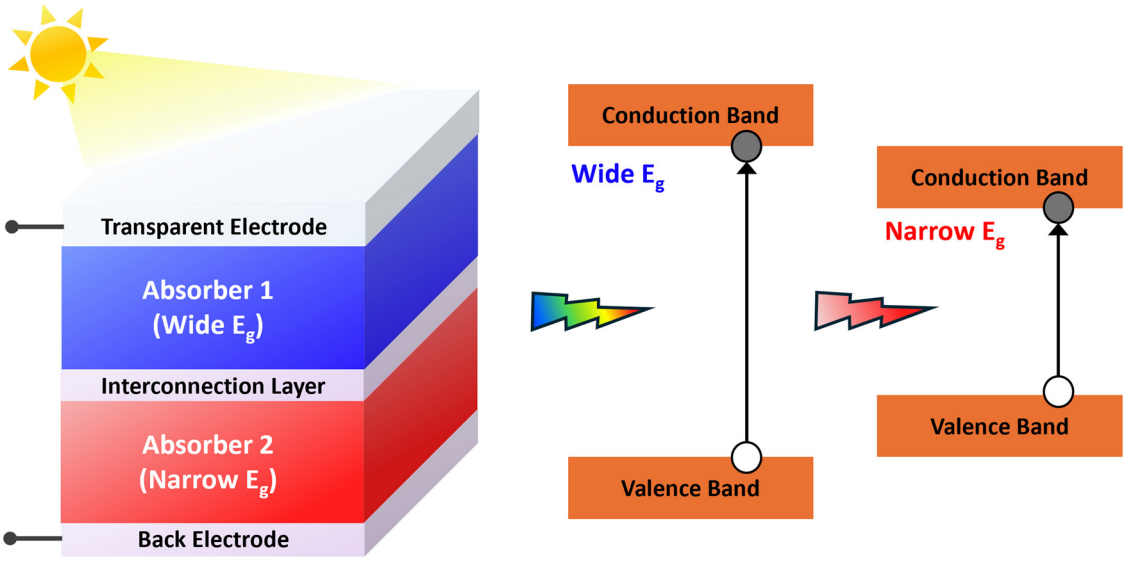

Types	Wide E_g (~1.5-1.8 eV)	Narrow E_g (~1.0-1.2 eV)	Advantage	Challenge
All-Perovskite	Perovskite	Perovskite	High Efficiency Low Cost	Low Stability
Perovskite/Silicon	Perovskite	Silicon	High Efficiency Good Stability	High Cost
Perovskite/Thin-Film	Perovskite	Thin Film	High Efficiency Good Stability	High Cost
Perovskite/Organic	Perovskite	Organic	Good flexibility Low Cost	Low Stability

Figure 1: Schematic illustration of T-SC architectures featuring a wide-bandgap top absorber (Absorber 1) and a narrow-bandgap bottom absorber (Absorber 2). The top cell efficiently harvests high-energy photons in the blue and green regions of the solar spectrum, while allowing red and NIR light to pass through to the bottom cell. The comparison includes four representative tandem configurations: All-perovskite, perovskite/silicon, perovskite/thin film, and perovskite/organic T-SCs.

telluride (CdTe) [7]), and perovskite/organic [8] configurations. In these architectures, a wide-bandgap perovskite top cell (Absorber 1) captures high-energy photons (blue and green light), while lower-energy photons (red and near-infrared [NIR]) pass through to a narrow-bandgap bottom cell (Absorber 2), as shown in Figure 1. Each combination presents distinct advantages and challenges. All-perovskite tandems are attractive due to their high-efficiency potential and relatively low cost; however, achieving long-term operational stability remains a significant hurdle. Perovskite/silicon tandems benefit from the mature and stable silicon platform and demonstrate excellent performance, yet face challenges related to fabrication complexity and cost. Perovskite/organic tandems are promising for their flexibility and low-cost fabrication of organic materials, but their efficiency and stability still require significant improvement. This review focuses on the emerging perovskite/CIGS T-SCs, which combine the high efficiency and bandgap tunability of perovskites with the proven stability and scalability of CIGS-based materials. This combination leverages the complementary strengths of both materials, offering a promising route toward cost-effective, high-performance, and durable tandem solar technologies.

Perovskite solar cells (PSCs) have garnered remarkable interest since their performance has achieved rapid efficiency improvements that have surpassed 26% in just a few years [9–16]. This remarkable progress is largely attributed to their outstanding optoelectronic properties, high absorption coefficients, tunable bandgaps, and compatibility with low-cost

solution-based fabrication processes. In particular, wide-bandgap perovskites (~1.6 eV) are well suited for use as top cells in T-SC architectures. When paired with CIGS solar cells, a mature and highly efficient thin-film technology (reaching up to 23.64% efficiency in single-junction devices), the resulting tandem configuration benefits from the complementary optical properties of both materials. The perovskite top cell efficiently absorbs high-energy photons (wavelengths below ~775 nm), while the CIGS bottom cell, with a narrower bandgap (~1.1 eV), captures lower-energy photons extending to ~1,100 nm. This division of the solar spectrum enables enhanced light harvesting and significantly improves the overall PCE. Studies have shown that optimizing the perovskite bandgap to ~1.6–1.7 eV, while maintaining the CIGS bandgap near 1.1 eV, results in ideal current matching and high efficiency, demonstrating over 24% for 2-terminal (2-T) and up to 28% for 4-terminal (4-T) configurations under standard AM 1.5G illumination.

Beyond spectral complementarity, CIGS contributes not only a favorable bandgap but also structural robustness and compatibility with flexible substrates, making it an excellent partner for perovskite-based tandems. These qualities broaden the application potential of tandem devices, especially in lightweight or portable PV systems. Despite these promising results, the long-term stability and environmental durability of perovskite/CIGS T-SCs remain key challenges. Perovskite materials are intrinsically sensitive to moisture, temperature fluctuations, and prolonged light exposure, all of which can lead to degradation. However, the incorporation of CIGS, known for its inherent stability, adds resilience to the overall tandem device, enhancing its potential for real-world applications.

Over the past decade, interest in PSCs has grown rapidly, reaching a peak of 6,073 journal publications in 2024. In contrast, research on CIGS solar cells remained relatively steady, averaging around 350 publications per year between 2014 and 2020. However, after 2020, CIGS-related publications declined, dropping to 208 in 2024. Notably, the T-SC approach combining PSC and CIGS solar cells has gained increasing attention, with publications on this topic rising from just 5 in 2015 to 25 in 2024. Correspondingly, citation counts have mirrored this upward trend, increasing from 46 in 2014 to 1,808 in 2024, reflecting growing interest and promising progress in tandem device research (Figure 2).

The economic viability of perovskite/CIGS T-SCs is another crucial aspect of their development. The potential to reduce the overall levelized cost of energy (LCOE), with low energy payback time (EPBT) and high return on energy invested (EROI) is a key indicator of sustainability for T-SCs. Furthermore, understanding the environmental impact of these technologies through lifecycle assessments will be essential in ensuring their sustainability and alignment with global climate goals.

This comprehensive review aims to discover recent advancements in the field of perovskite/CIGS T-SCs, focusing on key aspects such as the device architecture of each single junction, different configurations of T-SCs, including 2-T and 4-T configurations, the economic and environmental issues, and the challenges in the device architecture of the 2-T configuration. As the urgency for clean energy solutions increases, perovskite/CIGS T-SCs hold the potential to play a pivotal role in the renewable energy landscape, driving progress toward more efficient and sustainable solar energy systems.

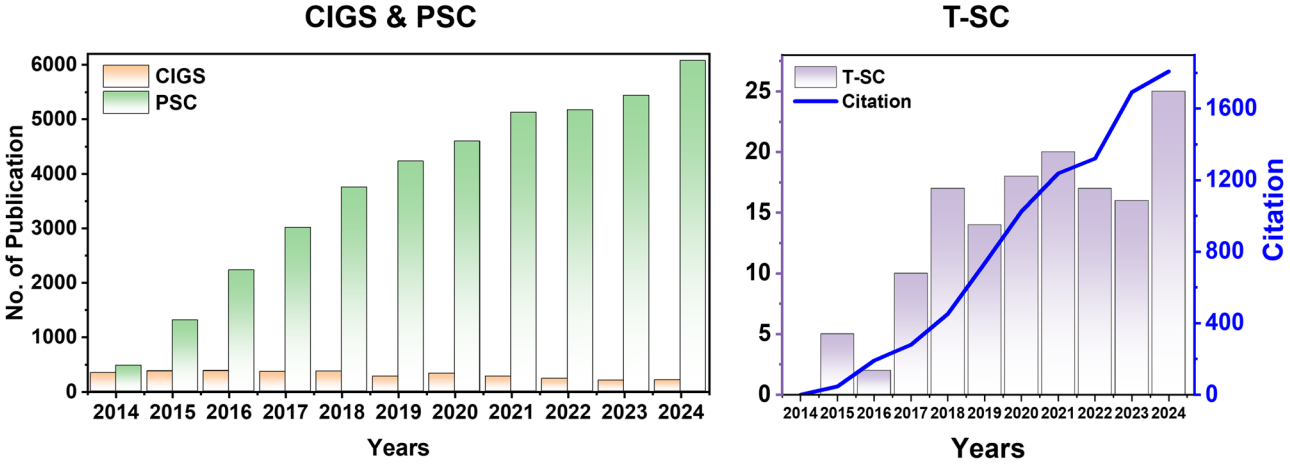

Figure 2: Annual publication trends for perovskite and CIGS solar cells (left) and T-SCs combining perovskite and CIGS technologies (right), including both publication and citation counts. Data obtained from the ISI Web of Science, covering the period from 2014 to 2024, and extracted on April 25, 2025.

2 Overview

2.1 PSCs

The term “perovskite” was first introduced by Russian mineralogist Lev A. Perovski to describe a specific crystal structure found in compounds like calcium titanate ($CaTiO_3$), with the general formula ABX_3. In this structure, the A-site hosts larger monovalent cations, such as cesium (Cs^+), rubidium (Rb^+), methylammonium (MA^+), or formamidinium (FA^+). The B-site represents smaller divalent metal cations, most commonly lead (Pb^{2+}), tin (Sn^{2+}), or germanium (Ge^{2+}). The X-site is occupied by anions, typically a halide like chloride (Cl^-), iodide (I^-), or bromide (Br^-), or other ions like thiocyanate (SCN^-) and tetrafluoroborate (BF_4^-). The ideal perovskite crystal structure forms a cubic lattice, where the B-site metal cation sits at the center of an octahedron, with the X-site positioned at the six vertices. The A-site cations occupy the space between these interconnected octahedra. This BX_6 octahedral coordination provides stability to the structure, as the B-cation is centrally coordinated by six X-anions, with the A-cations filling the gaps created by the adjoining octahedra.

As illustrated in Figure 3a, the A-site atom is located at the vertices, the B-site atom is at the center, and the X-site atoms occupy the face-centered positions [17]. This configuration results in a highly stable arrangement, where each A-site atom is surrounded by eight interconnected $[BX_6]^{4-}$ octahedra. The structural stability of perovskites depends on two key parameters: the Goldschmidt tolerance factor (t) and the octahedral factor (μ), which are essential for the formation of a stable perovskite structure. The Goldschmidt tolerance factor should fall within the range of $0.81 < t < 1.11$, while the octahedral factor must be between $0.44 < \mu < 0.90$. These factors can be calculated using equations (1) and (2), where r_A represents the atomic radius of the A atom, r_B represents the atomic radius of the B atom, and r_X represents the atomic radius of the X atom. Many different atomic species meet these criteria, enabling the formation of a wide variety of stable perovskite materials with tailored properties:

$$t = \frac{r_A + r_B}{\sqrt{2}(r_B + r_X)}, \quad (1)$$

$$\mu = \frac{r_B}{r_X}. \quad (2)$$

Perovskite materials offer a significant advantage in light absorption due to their high absorption coefficients, enabling them to capture sunlight effectively even in thin-film configurations [18–22]. In comparison, traditional silicon or germanium solar cells require much thicker absorbing layers to achieve comparable light absorption effects. This advantage is primarily due to the direct bandgap properties of perovskites, which facilitate efficient p–p transitions and enhance their light-harvesting capabilities, making them highly promising for PV applications (Figure 3b) [23,24]. Furthermore, as shown in Figure 3c, ion substitution within the perovskite crystal structure allows for precise tuning of the bandgap, offering control over the absorption spectrum. For example, replacing the A-site Cs^+ ions with the organic MA^+ ions or substituting the B-site Pb^{2+} ions with smaller Sn^{2+} ions leads to a redshift of the bandgap, while substituting the X-site I^- ions with smaller Br^- or Cl^- ions results in a blueshift. This tunable wavelength range, spanning from 400 to 1,000 nm, makes perovskites adaptable for various solar energy applications, perfectly matching the requirements for efficient light absorption across a broad spectrum [25,26].

Figure 3d-f presents three distinct structures of PSCs. Like other types of solar cells, including organic solar cells, PSCs consist of a photoactive layer, electrodes, an electron transport layer (ETL), and a hole transport layer (HTL). While the perovskite photoactive layer serves as the primary light-absorbing material, the ETL and HTL are critical for efficient charge transport, facilitating the movement of charge carriers to the electrodes. Numerous studies have focused on optimizing these transport layers to enhance charge collection and overall device performance [20,27–29]. Figure 3d illustrates the mesoporous n–i–p structure of PSCs. The ETL consists of dense titanium dioxide (TiO_2) and mesoporous TiO_2. The dense TiO_2 acts as the electron extraction layer, while the mesoporous TiO_2 not only supports the perovskite layer but also enhances light absorption by increasing the effective thickness of the perovskite layer. Additionally, a depletion zone forms at the interface between the dense TiO_2 and perovskite, which helps to prevent hole accumulation and minimize electron–hole recombination, ultimately improving the device performance. Figure 3e shows the planar n–i–p structure, which omits the mesoporous TiO_2 layer found in the mesoporous structure. The device is composed of a transparent conductive electrode (*e.g.*, FTO, ITO), the ETL (*e.g.*, TiO_2, tin(IV) oxide (SnO_2), barium stannate ($BaSnO_3$), zinc oxide (ZnO)), the perovskite absorption layer, an HTL (*e.g.*, 20,7,70-tetrakis[*N*,*N*-di(4-methoxyphenyl)amino]-9,90-spirobifluorene (Spiro-OMeTAD), poly[bis(4-phenyl)(2,4,6-trimethylphenyl)amine (PTAA), copper(I) thiocyanate (CuSCN)), and a top electrode (*e.g.*, Au, Ag). PSCs with this planar structure tend to exhibit higher open-circuit voltage (V_{OC}), but suffer from more pronounced hysteresis in the

current–voltage (*J*–*V*) curve [30]. Figure 3f shows the trans-planar p–i–n structure, where ETL and HTL swap positions compared to the planar structure. In this configuration, the device is structured from bottom to top as follows: transparent conductive electrodes (*e.g.*, FTO, ITO), HTL (*e.g.*, PTAA, PEDOT:PSS, NiO_x), perovskite absorption layer, ETL (*e.g.*, SnO_2, ZnO, PCBM), and top electrodes (*e.g.*, Au, Ag, Cu) [31]. The main advantages of this inverted-planar structure are its simplified fabrication process, low cost, and potential for use in tandem cell devices. However, it generally results in lower V_{OC} [32]. Table 1 summarizes recent PCSs devices that have achieved PCE greater than 25%, featuring both n–i–p and p–i–n structures, along with their corresponding thermal and light stability values.

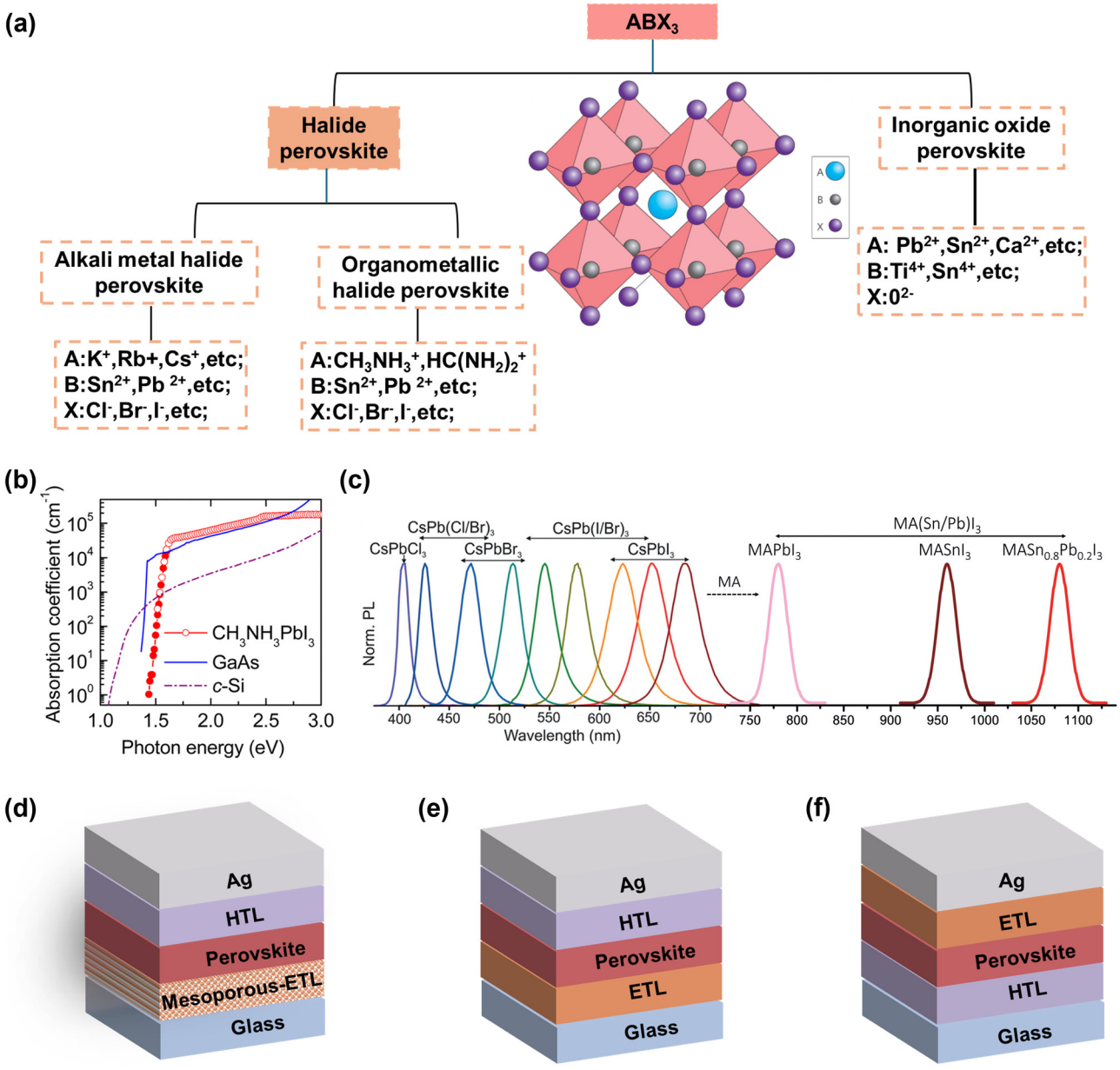

Figure 3: (a) Perovskite crystal structure of ABX_3, including both halide and inorganic oxide perovskites, with corresponding examples of elements for the A, B, and X sites. Also shown is an illustration of the ABX_3 perovskite structure. The cubic crystal structure is reproduced with permission from Green *et al.* [17]. Copyright 2014, Springer Nature. (b) The absorption coefficient of perovskite. Reproduced with permission from De Wolf *et al.* [23]. Copyright 2014, American Chemical Society. (c) The tunable bandgap of perovskite materials demonstrates how ion substitution can shift the absorption spectrum. Reproduced with permission from Saliba *et al.* [26]. Copyright 2018, John Wiley and Sons. Schematic illustrations of different device structure for PSCs: (d) mesoporous structure, (e) planar n–i–p, and (f) planar p–i–n structure.

2.2 CIGS solar cells

CIGS solar cells are based on a chalcopyrite crystal structure with a space group of I-42d. This structure is formed by substituting part of the indium (In) atoms in $CuInSe_2$(*CIS*) with gallium (Ga) atoms [51]. The crystal structure of CIGS is illustrated in Figure 4a, with lattice parameters c = 56~58 Å (x = 0–1) and a = 1.1–1.15 Å (x = 0–1). The lattice parameters vary with the In/Ga ratio, resulting in a tetragonal distortion caused by subtle differences in the bond lengths of Cu–Se, Ga–Se, and In–Se within the CIGS crystal [52,53]. Due to the varying electronegativity of Cu, In, and Ga atoms, the Cu–Se bond is typically shorter than the In–Se or Ga–Se bonds, leading to a slight distortion of the crystal structure that affects the lattice parameters a and c. As the Ga content increases, the presence of Ga–Se bonds causes an increase in the lattice parameter, while the variation in the *ccc*-axis is less pronounced (Figure 4b). This results in a reduction of the c/a ratio, causing a slight contraction of the crystal structure and an associated increase in the bandgap. Moreover, since Ga and In atoms can substitute for each other within the crystal lattice, the bandgap can be tuned by adjusting their relative proportions. This allows the bandgap to vary between 1.0 and 1.7 eV [52,54], optimizing the material's absorption of the solar spectrum. Generally, when the material has a higher In content and a lower Ga content, the bandgap is close to 1.0 eV, which favors the absorption of long-wavelength light and is suitable for the bottom layer of single-junction cells. In contrast, as the Ga content

Table 1: Device parameters with PCE exceeding 25% for single-junction PSC of n–i–p and p–i–n types, along with their thermal and light stability characteristics

Type	Year	Structure	J_{SC} (mA/cm^2)	V_{OC} (V)	FF (%)	PCE (%)	Thermal stability (h)	Light stability (h)	Ref.
n–i–p	2021	FTO/SnO_2/PVK/spiroMeOTAD/Ag	25.74	1.189	83.20	25.50	—	500	[33]
	2022	FTO/SnO_2/PVK/spiroMeOTAD/Ag	25.62	1.176	83.15	25.05	—	1,000	[34]
	2022	FTO/SnO2/PVK/spiroMeOTAD/Ag	25.72	1.123	86.90	25.09	500 (85°C)		[35]
	2022	ITO/SnO_2/PVK/spiroMeOTAD/Au	24.90	1.195	84.30	25.10	—	2,000	[36]
	2023	FTO/CsFo–SnO_2/$FAPbI_3$: $MDACl_2$/ spiro-OMeTAD/Au	24.91	1.173	85.65	25.03	120 (85°C)	380 (white LED)	[37]
	2023	FTO/c-TiO_2/PVK/spiro-OMeTAD/Au	26.04	1.181	82.21	25.30	500	>500 (25 °C 30–40% RH)	[38]
	2023	FTO/SnO_2/PVK/spiroMeOTAD/Ag	26.12	1.170	85.22	26.04	500 (85°C)	—	[10]
	2023	FTO/SnO2/PVK/spiroMeOTAD/Au	26.39	1.191	82.94	26.07	1,255	1,258 (50 ± 5°C)	[11]
	2024	FTO/c-TiO_2/PVK/o-F-PEAI//Au	25.90	1.174	83.26	25.32	300 (85°C 85% RH)	500 (1.5 G)	[39]
	2024	FTO/SnO_2/PVK/spiroMeOTAD/ MoO_3/Ag	25.80	1.167	84.39	25.41	—	1,100 (white LED)	[40]
	2023	FTO/SnO_2/PVK/spiroMeOTAD/Au	25.69	1.178	86.15	26.08	—	600 (encapsulated)	[9]
	2024	ITO/SnO_2/PVK/spiroMeOTAD/Au	25.92	1.173	85.82	26.11	>900 (55°C)	—	[16]
	2024	FTO/SnO_2/PVK/Spiro-OMeTAD/Au	26.47	1.175	84.94	26.41	1,500 (65°C)	600	[15]
	2025	FTO/SnO_2/PVK/Spiro-OMeTAD/Au	26.05	1.159	83.65	25.27	700 (65°C)	2,500	[41]
	2025	FTO/SnO_2/PVK/Spiro-OMeTAD/Au	26.33	1.158	83.77	25.54	200 (85°C)	2,000	[42]
p–i–n	2022	ITO/Me-2PACZ/PVK/LiF/C_{60}/BCP/Ag	26.13	1.150	84.60	25.49	850 (85°C 85% RH)	2,400 (55°C)	[43]
	2023	ITO/MPA-CPA/PVK/C_{60}/BCP/Ag	24.80	1.210	84.70	25.40	500	500 (45°C 30-40% RH)	[44]
	2023	ITO/Me-4PACZ/PVK/LiF/C_{60}/BCP/Ag	25.08	1.208	84.37	25.56	1,000 (85°C)	1,000	[45]
	2023	ITO/NiO_x/MeO-4PADBC/PVK/C_{60}/ BCP/Ag	25.40	1.190	84.60	25.60	—	1,200 (65°C)	[46]
	2023	ITO/PTAA/PVK/C_{60}/BCP/Ag	26.14	1.164	85.74	26.10	350 (85°C 85% RH)	2,500	[12]
	2024	FTO/NiO_x/NCS/PVK/PCBM/BCP/Ag	24.83	1.170	86.24	25.05	700 (85°C, N_2)	1,700	[47]
	2024	ITO/NiO_x/PTAA/AlOx/PVK/BCP/Ag	26.11	1.184	84.20	26.03	1,500 (85°C 85% RH)	2,500	[48]
	2024	FTO/SAMs/PVK/C_{60}-SnO_2/Ag	26.13	1.174	85.2	26.15	1,200	1,500	[14]
	2025	ITO/Ph-4PACz/PVK/C_{60}/BCP/Ag	25.70	1.202	85.39	26.38	700 (65°C, N_2)	800	[49]
	2025	ITO/MeO-2PACz/PVK/C_{60}/BCP/Cu	26.29	1.176	85.90	26.57	1,100 (85°C, N_2)	1,200	[50]

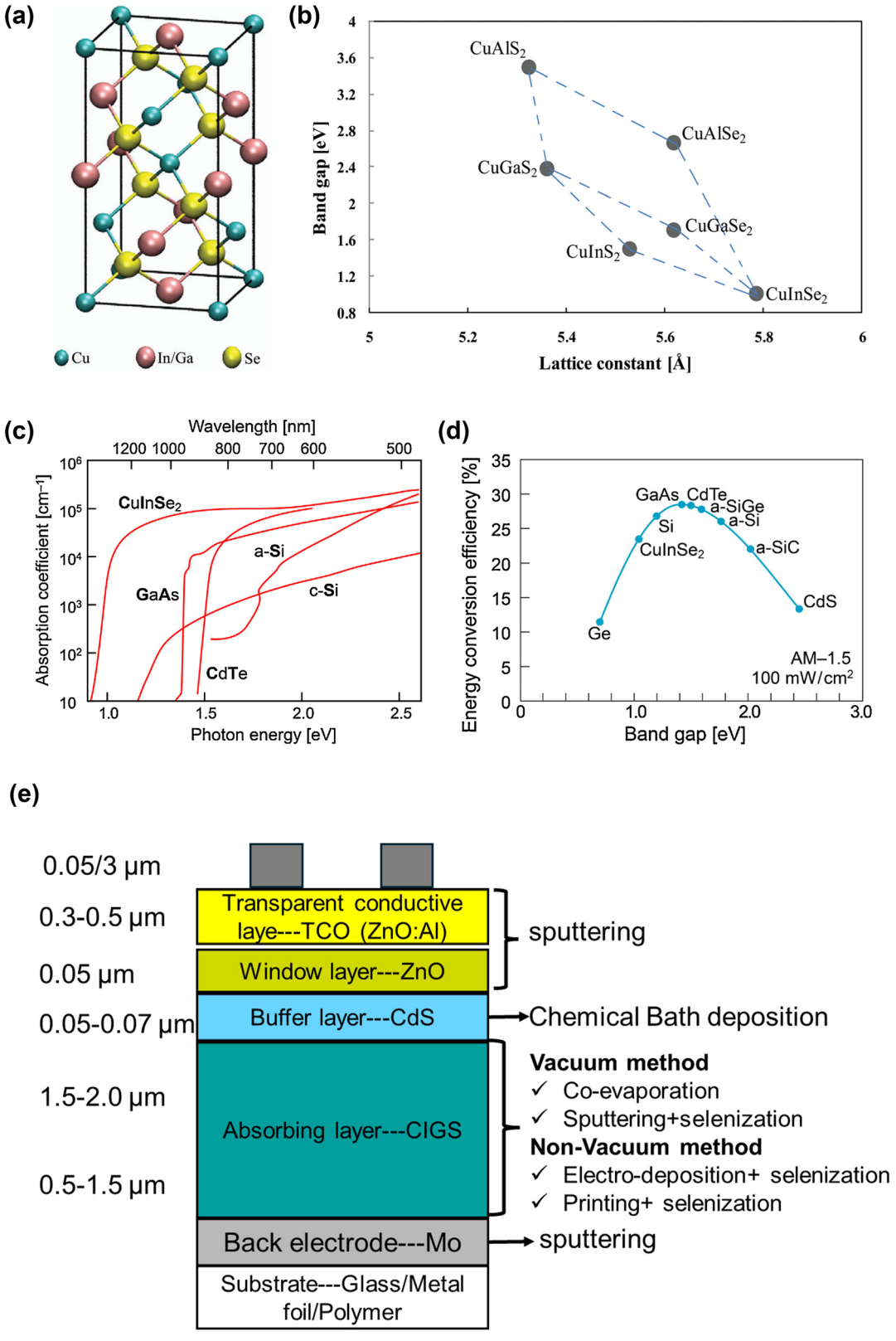

Figure 4: (a) Crystal structure of the tetragonal chalcopyrite CIGS unit cell. Reproduced with permission from Ghorbani *et al.* [59]. Copyright 2015, American Chemical Society. (b) Bandgap as a function of lattice constant *a* of the Cu(In, Ga, Al)(S, Se)$_2$ alloy system. Reproduced with permission from Ramanujam and Singh [58]. Copyright 2017, Royal Society of Chemistry. (c) Relationship between the absorption coefficient and the photon energy for different materials, and (d) theoretical energy conversion efficiencies of commercial thin film solar modules. Reproduced with permission from Chandra *et al.* [56]. Copyright 2014, Elsevier. (e) Device structure of CIGS solar cells.

increases, the bandgap widens to approximately 1.7 eV, making it more effective for absorbing short-wavelength light, a property desirable for the top layer of tandem cells [55]. This tunable bandgap characteristic not only enhances the material's sensitivity to different regions of the solar spectrum but also reduces energy losses of photogenerated carriers, thereby improving the PV conversion efficiency. As a result, CIGS materials exhibit an exceptionally high optical absorption coefficient, enabling the absorption of most visible light even within ultra-thin films as thin as ~1 μm (Figure 4c). This efficient absorption facilitates the generation of electron–hole pairs within a very thin absorber layer, significantly enhancing the photoelectric conversion efficiency (Figure 4d) [56].

CIGS thin-film solar cells represent a highly efficient PV technology, typically composed of multiple functional layers. The substrate provides mechanical support for the cell and is commonly made of glass, metal, or plastic [57]. On top of the substrate, the back electrode layer, usually composed of molybdenum (Mo), facilitates the extraction of electric current. The absorber layer, which forms the core of the cell, is a compound thin film composed of Cu–In–Ga–Se. This layer is responsible for absorbing sunlight and converting it into an electrical current. It exhibits exceptional light absorption properties, enabling effective solar energy harvesting even with relatively thin film thicknesses. To optimize charge separation and enhance cell efficiency, a buffer layer, such as cadmium sulfide (CdS), is typically positioned between the CIGS absorber layer and the transparent conductive oxide (TCO) layer. The TCO layer, made of materials like indium tin oxide (ITO) or ZnO, forms the outermost layer of the cell. It is both electrically conductive and optically transparent, allowing the collection of photogenerated electrons while permitting the transmission of light. Finally, the front electrode, connected to the TCO layer, serves as the output terminal, collecting the electrical current generated by the absorber layer, as shown in Figure 4e [58]. Table 2 summarizes the CIGS device parameters over the years from 2011 to 2025.

3 Device configuration of tandem perovskite/CIGS solar cells (T-SCs)

Both perovskite and CIGS represent advanced thin-film technologies that can be effectively combined into T-SCs. The combination bandgaps of perovskite and CIGS improve the absorption of a broader range of the solar spectrum, making their combination a promising approach to increase the overall efficiency of solar devices. In the perovskite/CIGS tandem system, PSCs are positioned above CIGS cells, as the bandgap of perovskite can be tuned to a higher energy, enabling more effective utilization of

Table 2: Device structure and performance of CIGS solar cells

Year	Structure	J_{SC} (mA/cm^2)	V_{OC} (V)	FF (%)	PCE (%)	Ref.
2011	Glass/Mo/CIGS/CdS/ZnO:Al(ZnO)/Ni-Al grid/MgF_2	35.4	0.740	77.5	20.3	[60]
2013	Polyimide film/Mo/CIGS/CdS/ZnO:Al(ZnO)/Ni-Al-Ni grid/MgF_2	35.1	0.736	78.9	20.4	[61]
2014	Glass/Mo/CIGS/CdS/ZnO:Al(ZnO)/Ni-Al grid/MgF_2	36.6	0.746	79.1	20.8	[62]
2015	Glass/Mo/CIGS/CdS/ZnO:Al(ZnO)/Ni-Al-Ni grid	36.6	0.746	79.3	21.7	[63]
2016	Glass/Mo/CIGS/CdS/ZnO:B(ZnO)/Al/MgF_2	39.4	0.721	78.2	22.3	[64]
2016	Glass/Mo/CIGS/CdS/(Zn,Mg)O or ZnO:Al(ZnO)/Ni-Al-Ni grid	37.8	0.741	80.6	22.6	[65]
2019	Glass/Mo/CIGS/CdS/ZnO:Al(ZnO)/Ni-Al grid	36.6	0.731	75.9	20.3	[66]
2019	Glass/Mo/CIGS/CdS/ZnO:Al(ZnO)/MgF_2	35.03	0.770	77.5	20.9	[67]
2019	Glass/Mo/Mo(S,Se)/CIGSSe/CdS or Zn(O,S,OH)x/$Zn_{0.8}Mg_{0.2}O$(ZMO)/ZnO:B(ZnO)/Al/MgF_2	39.6	0.734	80.4	23.4	[68]
2019	Glass/Mo/CIGS/B(ZnO)/MgF_2	38.5	0.746	79.7	22.9	[69]
2020	SLG/Mo/CIGS/CdS/AZO:i-ZnO/NiO/Al	36.49	0.635	70.6	16.4	[70]
2020	Glass/CIGS/CdS/Al(ZnO)/Antireflection coating/Ag Grid	33.8	0.755	79.2	20.2	[71]
2020	Glass/Mo/CIGS/CdS/(Zn,Mg)O:Al(ZnO)/Ni–Al grid	36.3	0.741	80.2	21.6	[72]
2021	Indium/GaAs/CIGS/CdS/Al(ZnO)/Antireflection coating/Ag Grid	34.6	0.74	80	20.4	[73]
2021	Glass/Mo/CIGS/CdS/(Zn,Mg)O:Al(ZnO)/Ni–Al–Ni grid	36.6	0.720	79	20.8	[74]
2022	Glass/Mo/CIGS/CdS/ZnO:Al(ZnO)/Ni–Al–Ni grid/MgF*2*	37.35	0.746	76.69	21.4	[75]
2023	SLG/Mo/CIGS/CdS/AZO:i-ZnO/MgF_2/Al grid	34.7	0.774	79.5	21.4	[76]
2024	Glass/Mo/CIGS/CdS/Al(ZnO)/MgF_2/Ni–Al grid	34.7	0.785	80.6	22.0	[77]
2024	Glass/Mo/NaF-precursor/ACIGS/RbF-PDT/CdS/i-ZnO/ZnO:Al/MgF_2	38.3	0.7671	80.46	23.6	[78]
2025	Glass/Mo/CIGS/CdS/i-ZnO/ITO/Ag MgF_2	32.8	0.662	75.8	16.48	[79]

sunlight. T-SCs can be fabricated in two ways: by depositing all layers of top cells directly onto the bottom cells in a 2T configuration, or by mechanically stacking two independent solar cells in a 4-T configuration, as illustrated in Figure 5a, along with their equivalent circuit in Figure 5b.

In the 2-T design of T-SCs, a streamlined structure minimizes complexity and cost while maximizing light absorption and energy conversion efficiency. The 2-T T-SCs consist of two distinct PV layers – an upper perovskite layer and a lower CIGS layer – fabricated on a common substrate. Within this 2-T structure, the sub-cells are linked together through an interconnection layer or tunnel junction within a single monolithic device. In this configuration, both layers are electrically connected in series, allowing the current generated by the upper perovskite top cell to pass through the lower CIGS bottom cell. This series connection enables the tandem device to leverage the broad absorption spectrum of both materials, capturing more sunlight than either cell could achieve independently. The combined current from both layers flows through the external circuit, resulting in higher overall efficiency compared to standalone devices. Conversely, the 4-T configuration consists of two distinct PV cells – an upper PSC and a lower CIGS cell – each connected to its own set of electrodes. This configuration allows for independent operation of each cell, facilitating optimized performance and better management of charge carriers. The independent operation allows for optimized performance and flexibility in circuit design, making it easier to adapt the tandem cell for various applications, including integration into existing solar technologies.

Figure 5c (adapted from Eperon *et al.*) presents theoretical maximum efficiency contour maps for 2-T and 4-T T-SCs, with dashed lines indicating peak efficiency across a range of top cell bandgaps and dots representing global maximum PCEs [80]. Notably, the highest PCEs for both tandem configurations can exceed 46% under 1 sun illumination. In the 2T configuration, however, the need for current matching imposes a stricter limit on the top cell bandgap, typically ranging from 1.5 to 1.9 eV for optimal PCE. In contrast, the 4-T configuration allows each sub-cell to operate at its maximum power point (MPP), providing a wider selection of bandgap combinations.

The *J*–*V* parameters for various T-SCs configurations are summarized in Table 3, offering a comprehensive comparison of their performance characteristics and efficiencies. Lead halide perovskites, with tunable bandgaps ranging from 1.5 to 2.2 eV, are particularly well-suited as a top cell in both 2-T and 4-T architectures due to their strong light absorption and bandgap flexibility. When comparing the performance of these configurations, the PCE of 2-T has shown relatively limited progress, remaining in the range of approximately 20 to 24% from 2019 to 2025. The highest reported PCE for a 2-T perovskite/CIGS tandem was achieved by Geng *et al.*, reaching 24.6% in 2025 [83]. In contrast, 4-T configurations have demonstrated significantly higher performance potential, with the highest reported PCE reaching 30.10% by Tian *et al.* [84]. The comparatively lower efficiencies observed in 2-T configurations are primarily attributed to several key challenges. These include suboptimal bandgap alignment between the wide-bandgap perovskite top cell and the narrower-bandgap CIGS bottom cell, which impairs current matching and is a crucial requirement for efficient 2-T operation. Additionally, the development of high-quality tunnel junctions and effective charge-selective interlayers remains a significant technical barrier. Material compatibility at the perovskite/CIGS interface also presents issues, often leading to interfacial defects, accelerated degradation, and compromised device stability.

Todorov *et al.* developed the first 2-T perovskite/CIGS T-SC with a structure of Ca/BCP/PCBM/perovskite/PEDOT:PSS/ITO/CdS/CIGS/Mo/Si_3N_4/glass in September 2015 [85]. Notably, the intrinsic ZnO layer, typically used in CIGS devices, was omitted due to its incompatibility with the perovskite layer. Instead, a 30 nm-thick ITO film, deposited on CdS *via* sputtering, was selected as the transparent recombination layer. To optimize the perovskite sub-cell, an $MAPbI_xBr_{3-x}$ absorber was prepared by controlled evaporation of MABr onto a solution-processed $MAPbI_3$ film. The back sub-cell employed a CIGS absorber with a bandgap of 1.04 eV, while the perovskite bandgap was varied between 1.65 and 1.75 eV. Ultimately, a 1.72 eV bandgap yielded the best performance, resulting in a monolithic tandem device with an efficiency of 10.98%. However, this performance is lower than of the individual sub-cells, with the single-cell PSC and the single-cell CIGS achieving 11.4% efficiency, primarily due to the 70–80% transmittance of the Ca/BCP-based front contact. Although the performance is reduced, the V_{OC} of the T-SCS increases to 1.45 V, demonstrating that the monolithic integration of perovskite and CIGS is achievable.

Han *et al.* addressed surface roughness in perovskite/CIGS T-SCs by sputtering a thick ITO recombination layer onto the CIGS bottom cell, followed by polishing to reduce roughness [86]. This approach enabled spin coating of the perovskite and thin contact layers without significant losses caused by surface irregularities. As a result, they achieved a PCE of 20.8% on a 0.52 cm^2 device, with a certified PCE of 22.4% on a smaller 0.042 cm^2 area. The device demonstrated a high V_{oc} of 1.78 V. However, the use of a thick ITO layer increased free carrier absorption in the NIR

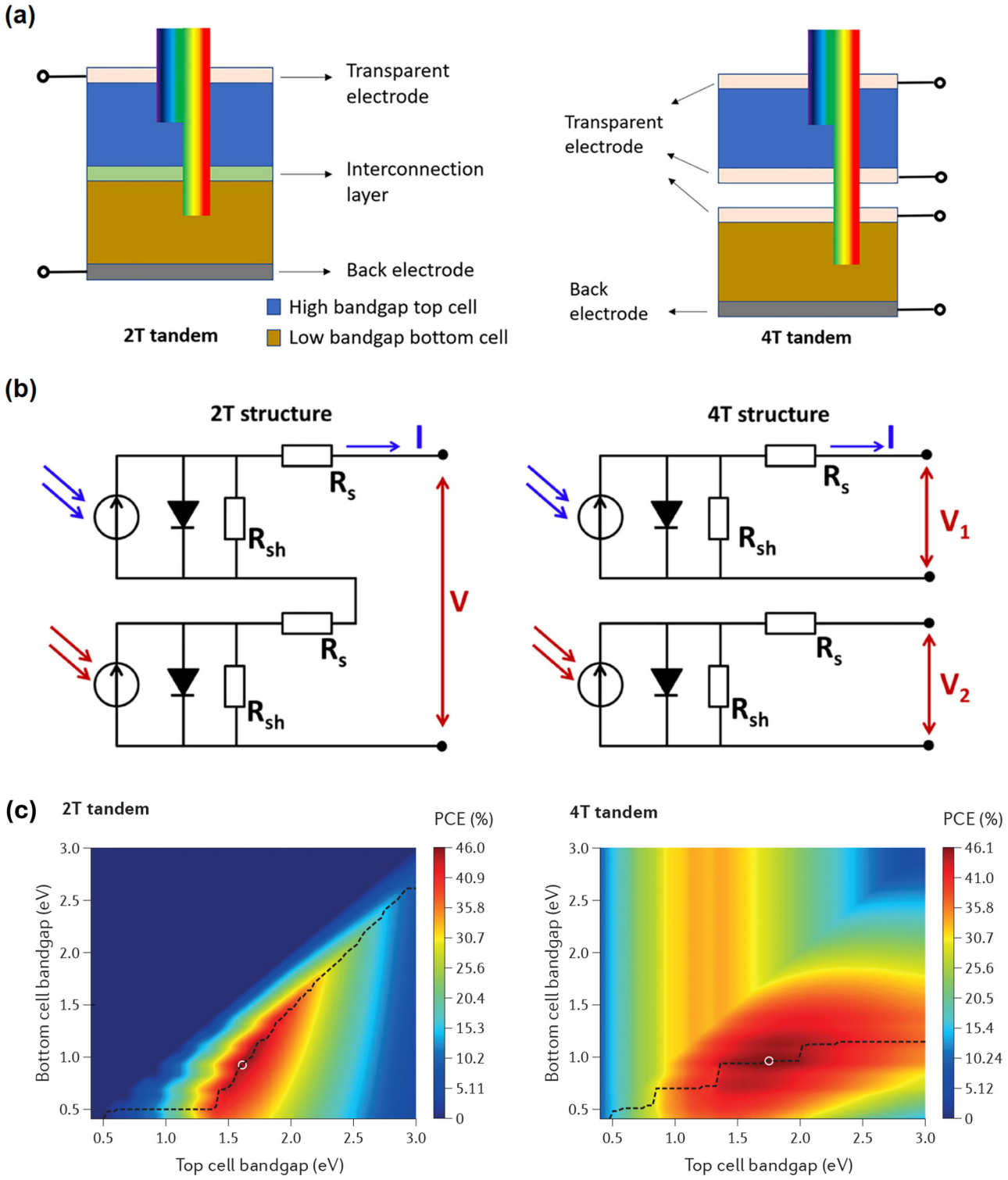

Figure 5: (a) Device structures for 2-T and 4-T T-SCS configurations. Reproduced under the term of the CC-BY license [81]. Copyright 2021, Baillie, A.W.Y., AIP Publishing. (b) Equivalent circuits for 2-T and 4-T T-SCS under illumination, highlighting shunt resistance (R_{sh}), series resistances (R_s), output voltage (V), and output current (I). Reproduced under terms of the CC-BY license [82]. Copyright 2021, Y. Cheng and L. Ding, John Wiley and Sons. (c) Theoretical maximum PCE for 2-T and 4-T T-SCs. Reproduced with permission from Eperon *et al.* [80]. Copyright 2017, Springer Nature.

Table 3: Summary of *J–V* parameters for 2-T and 4-T T-SCs

Year [ref]	Configuration	Eg (eV)	*V*oc (V)	*J*sc (mA/cm^2)	FF (%)	Area (cm^2)	PCE (%)	Total PCE (%)	Ref.
2-T Configuration									
2015	PSC	1.72	1.01	16.1	70.2	—	11.40		[85]
	CIGS	1.04	0.47	36.5	66.8	—	11.40		
	2T-SCs (Ca/BCP/PCBM/MAPbBr$_x$I$_{3-x}$/PEDOT:PSS/ITO/CdS/CIGS/Mo)	—	1.45	12.7	56.6	0.40	10.98		
2018	PSC	1.59	1.09	18.2	75.5	—	14.95		[86]
	CIGS	1.0	0.67	34.3	72.4	—	16.76		
	2T-SCs (MgF_2/ITO/ZnO/PCBM/$Cs_{0.09}FA_{0.77}$ $MA_{0.14}Pb(I_{0.86}Br_{0.14})_3$/PTAA/ITO/BZO/iZO/CdS/CIGS/Mo)	—	1.77	17.3	73.1	0.04	22.43		
2019	PSC	1.6	1.09	20.4	74.8	—	16.70		[87]
	CIGS	1.1	0.65	35.8	70.6	—	16.30		
	2-T-SCs (LiF/Ag/IZO/SnO_2/C_{60}/$Cs_{0.05}(MA_{0.17}FA_{0.83})Pb_{1.1}(I_{0.83}Br_{0.17})_3$/PTAA/$NiO_x$/AZO/iZO/CdS/CIGS/Mo)	—	1.58	18.0	75.7	0.81	21.60		
2019	PSC	—	1.14	22.2	80.5	—	20.40		[88]
	CIGS	—	—	—	—	—	16.30		
	2-T-SCs (LiF/Ag/IZO/SnO_2/C_{60}/$Cs_{0.05}(MA_{0.17}FA_{0.83})_{0.95}Pb(I_{0.83}Br_{0.17})_3$/MeO-2PACz/AZO/iZO/CdS/RbF/CIGS/Mo)	—	1.68	19.2	71.9	1.03	23.26		
2022	PSC	—	—	—	—	—	—		[5]
	CIGS	—	—	—	—	—	—		
	2-T-SCs (LiF/IZO/SnO_2/C_{60}/LiF/$Cs_{0.05}MA_{0.23}FA_{0.77}Pb(I_{0.77}Br_{0.23})_3$/Me-4PACz/AZO/iZO/CdS/CIGS/Mo)	—	1.77	18.8	71.2	1.04	24.20		
2023	PSC	1.63	—	—	—	—	—		[89]
	CIGS	1.06	—	—	—	—	—		
	2-T-SCs (Ag/LiF/IZO/SnO_2/C_{60}/$Cs_{0.05}(MA_{0.17}FA_{0.83})_{0.95}Pb(I_{0.83}Br_{0.17})_3$/$NiO_x$(:Cu) + MeO-2PACz/AZO/i-ZnO/CdS/CIGS/Mo/)	—	1.63	19.2	69.1	1.08	21.60		
2024	PSC	—	—	—	—	—	—		[90]
	CIGS	—	—	—	—	—	—		
	2-T-SCs (ITO/SnO_X/$Cs_{0.05}FA_{0.77}MA_{0.18}Pb(I_{0.82}Br_{0.18})_3$/Spiro-OmeTAD/TCA/$AlO_X$/ITO/ZnO:Al/ZnMgO/InS:Na/CIGS/Mo)	—	1.78	17.7	66.3	—	20.80		
2025	PSC	—	—	—	—	—	—		[83]
	CIGS	—	—	—	—	—	—		
	2-T-SCs (LiF/Ag/IZO/C_{60}/SnO_X/LiF/$Cs_{0.05}(FA_{0.83}MA_{0.17})_{0.95}Pb(I_{0.83}Br_{0.17})_3$/2PACz/$NiO_x$/IZO/CIGS/Mo)	—	1.74	21.0	67.3	0.16	24.60		
4-T Configuration									
2015	LiF/glass/FTO/c-TiO_2/mp-TiO_2/$MAPbI_3$/spiro-/AgNW/LiF	1.55	1.03	17.5	71.0	0.39	12.70	18.6	[91]
	Mo/CIGS/CdS/iZO/AZO/NiAl/MgF_2	—	0.68	10.9	78.8	—	5.90		
2015	Glass/FTO/ZnO/PCBM/$MAPbI_3$/spiro-/MoO_3/IO:H/NiAlNi	1.55	1.10	17.4	73.6	0.52	14.10	20.5	[92]
	Mo/CIGS/CdS/iZO/AZO/NiAlNi	—	0.67	12.7	74.9	—	6.30		
2016	Glass/IO:H/PTAA/$MAPbI_3$/PCBM/ZnO/AZO/NiAl	1.55	1.12	19.1	75.4	0.21	16.10	22.1	[93]
	Mo/CIGS/CdS/iZO/AZO/NiAlNi	—	0.67	12.1	73.6	—	6.00		
2017	Glass/FTO/c-TiO_2/mp-TiO_2/$Cs_{0.05}(MA_{0.17}FA_{0.83})_{0.95}Pb(I_{0.83}Br_{0.17})_3$/spiro-/Ag/ITO	—	0.98	20.1	78.1	0.09	16.0	20.7	[94]
	Mo/CIGS/CdS/ITO	—	0.47	15.2	64.6	—	4.70		
2018	$Cs_{0.05}Rb_{0.05}FA_{0.765}MA_{0.135}PbI_{2.55}Br_{0.45}$	1.62	1.14	21.8	74.0	0.30	18.4	23.9	[95]
	CIGS	—	0.62	13.0	72.0	0.50	5.60		
	$Cs_0.Rb_{0.05}FA_{0.75}MA_{0.15}PbI_{1.8}Br_{1.2}$	1.75	1.19	19.3	71.0	0.30	16.0	23.4	
	CIGS	—	1.63	15.8	74.2	0.50	7.40		
2020	ARC/glass/FTO/c-TiO_2/m-TiO_2/$K_{0.05}(FA_{0.85}MA_{0.115})_{0.95}Pb(I_{0.85}Br_{0.15})_3$/spiro-/Au	—	1.18	21.0	77.2	1.00	19.10	28.0	[96]
	Mo/CIGS/Zn(O,S,OH)ZMO/BZO/Al/MgF_2	—	0.64	18.4	75.8	—	8.90		
2022	MgF_2/glass/IO:H/2PACz/$Cs_{0.17}FA_{0.83}Pb(I_{0.92}Br_{0.08})_3$/LiF/$C_{60}$/$SnO_x$/IZO/$MgF_2$	—	1.17	20.9	76.0	0.08	18.5	27.3	[97]

(*Continued*)

Table 3: *Continued*

Year [ref]	Configuration	Eg (eV)	*V*oc (V)	*J*sc (mA/cm^2)	FF (%)	Area (cm^2)	PCE (%)	Total PCE (%)	Ref.
	Mo/CIGS/CdS/ZMO/AZO/NiAlNi/MgF_2	—	0.66	17.7	78.6	—	8.80		
2023	MgF_X/ITO/Poly-TPD/$FA_{0.78}Cs_{0.22}Pb(I_{0.82}Br_{0.15}Cl_{0.03})_3$/$C_{60}$/$SnO_x$/IZO	1.67	1.20	19.5	81.4	—	19.07	28.4	[98]
	Mo/CIGS/CdS/i-ZnO/AZO	1.04	0.60	20.3	75.4	—	9.30		
2024	Glass/ITO/MeO-4PACz/$Cs_{0.05}(FA_{0.77}MA_{0.23})_{0.95}Pb(I_{0.77}Br_{0.23})_3$/$C_{60}$/BCP/Ag	—	1.18	20.4	84.0	—	20.30	29.1	[99]
	Mo/CIGS/CdS/i-ZnO/AZO	—	0.59	20.6	72.7	—	8.83		
2025	Glass/ITO/NiO_x/$Cs_{0.05}(FA_{0.76}MA_{0.14})_{0.95}Pb(I_{0.76}Br_{0.24})_3$/LiF/$C_{60}$/$SnO_2$/IZO	1.68	1.25	20.7	84.7	0.09	21.88	30.1	[84]
	Mo/CIGS/CdS/i-ZnO/AZO	—	0.64	17.6	72.7	—	8.25		

region, reducing the current generated in the CIGS bottom sub-cell. This was evidenced by a low short-circuit current density (J_{sc}) of 17.3 mA/cm^2 in the tandem configuration.

In contrast, Jošt *et al.* adopted an alternative strategy, avoiding polishing by conformally depositing an HTL directly onto the as-grown rough CIGS surface [87]. Using atomic layer deposition (ALD), they applied a 10 nm NiO_x layer that formed a uniform, closed coating, as confirmed by TEM cross-section measurements. By comparison, a spin-coated PTAA polymer layer with the same nominal thickness failed to cover the peaks of the rough surface, leading to agglomeration in the valleys and poor performance in PTAA-only devices. The NiO_x layer prevented shunting in the top cell, achieving a PCE of 18.0%. Furthermore, the combination of NiO_x with PTAA (forming a NiO_x/PTAA bilayer) improved the interface between NiO_x and the perovskite layer, enhancing performance. This bilayer approach achieved a PCE of 21.6% over a larger area of 0.78 cm^2.

Bailie *et al.* employed silver nanowires (AgNWs) as a transparent electrode for flexible perovskite sub-cells, achieving a high transparency of 90% in the 530–730 nm range. When combined with a 17% CIGS rear sub-cell, the tandem device reached an overall efficiency of 18.6% [91]. Later, Lee *et al.* adopted AgNWs for a fully solution-processed $MAPbI_3$/CIGS device [100]. While this approach reduced manufacturing costs, it yielded a modest efficiency of 10%, reflecting the challenges associated with AgNWs, such as processing complexity and solvent-induced performance variability. To explore alternative transparent electrodes, two notable studies were published in June 2015 by Tiwari and Yang's groups [101,102]. Tiwari's group proposed a sputtered ZnO:Al TCO layer, resulting in a device structure of FTO/TiO_2/$MAPbI_3$/Spiro/MoO_3/ZnO:Al + CIGS, achieving an overall efficiency of 19.5%. In contrast, Yang's group developed a dielectric–metal–dielectric (DMD) structure using MoOx/Au/Ag/MoOx as transparent contacts, yielding an efficiency of 15.5% with a structure of DMD/Spiro-OMeTAD/$MAPbI_3$/TiO_2/ITO + CIGS. Building on these advancements, Fu *et al.* demonstrated notable improvements in 4-T T-SCs [92,93]. In 2015, they sputtered a semi-transparent In_2O_3:H rear electrode onto a spin-coated $MAPbI_3$ PSC with an efficiency of 14.2%. When combined with a CIGS bottom cell, the 4-T tandem device achieved an efficiency of 20.5% over an illumination area of 0.517 cm^2. Further refinement in 2016 included the use of ZnO:Al and In_2O_3:H as front and rear contacts, boosting the perovskite top cell efficiency to 16.1% and achieving an overall tandem efficiency of 22.1%. In another breakthrough, Guchhait *et al.* demonstrated a triple-cation $Cs_x(MA_{0.17}FA_{0.83})_{(100-x)}Pb(I_{0.83}Br_{0.17})_3$ perovskite-based semitransparent device with an Ag/ITO back contact, achieving a PCE of 16%. When paired with a CIGS bottom cell in a 4-T configuration, the overall tandem efficiency reached 20.7% [94]. Further advancements were reported in 2018 by Shen *et al.*, who developed a multijunction solar cell with a record-breaking efficiency of 23.9%. This exceeded the efficiencies of single-junction CIGS (22.6%) and single-junction PSCs (18.4%) [95]. Their approach incorporated a Cs/Rb/FA/MA wide-bandgap perovskite layer and a 140 nm indium–zinc oxide (IZO) transparent electrode, with MoOx as a buffer layer and a metal grid to enhance conductivity. The semi-transparent perovskite cell displayed excellent transparency in the 700–800 nm range, a critical factor enabling the high efficiency of the multijunction configuration.

Table 4 summarizes the key differences between 2-T and 4-T T-SC configurations, focusing on efficiency, manufacturing complexity, and device integration. 2-T tandem cells are generally more efficient and easier to manufacture, making them a more attractive option for

commercialization. By connecting the two sub-cells in series, 2-T cells achieve higher PCE, utilizing a larger portion of the solar spectrum with reduced system complexity and lower costs. Additionally, the series configuration simplifies current matching between sub-cells, which is a key advantage for scalability and mass production. In contrast, while 4-T configurations offer greater flexibility in design, they tend to suffer from lower efficiency due to energy losses from the independent electrical circuits and the complexity of managing separate outputs for each sub-cell. Moreover, challenges in finding ideal transparent electrodes for 4-T cells can lead to parasitic absorption and reflection losses, contributing to optical inefficiencies. Overall, while 4-T tandem cells offer some advantages in design flexibility and voltage matching, the simplicity, efficiency, and cost-effectiveness of 2-T configurations make them more promising for mass commercialization.

4 Economic and environmental perspectives

4.1 Economic aspects

The development of T-SCs has garnered significant attention due to their potential for high efficiency and relatively low manufacturing costs. From an economic perspective, T-SCs offer both challenges and opportunities, particularly in reducing costs, enhancing scalability, and promoting market adoption. A key economic advantage is their potential to lower the overall LCOE, a critical metric for evaluating the cost-effectiveness of electricity generation. LCOE accounts for the per-unit cost of building and operating a power plant over its expected lifetime, making it a central consideration for the energy industry [103].

The tandem configuration boosts the overall PCE, potentially exceeding 30%, which translates to more electricity generated per square meter of solar panel. Higher efficiency means that fewer panels are needed to meet the same energy demand, which directly reduces the installed cost and, ultimately, the LCOE. The overall manufacturing cost of T-SCs can vary based on the materials and fabrication technique employed. Generally, these costs tend to be higher than those of single-junction cells, mainly due to the inclusion of additional layers such as charge transport or buffer layers in 2T configurations and transparent electrodes in 4T designs. These added components can increase the complexity of production and raise costs. However, the cost increase associated with these extra layers is relatively small compared to the combined manufacturing cost of the two separate devices, primarily because of the reduction in balance-of-system (BOS) components, such as the glass, frame, laminating film, and junction box. These BOS components typically account for around 60–85% of the total cost. In contrast, the cost associated with the materials used for the active layer fabrication constitutes only 6–23% of the total cost [104].

As illustrated in Figure 6a, the manufacturing cost of a perovskite single-junction solar cell is the lowest at 27.18 US $/m^2, followed by the CIGS single-junction at 38.25 US $/m^2,

Table 4: Comparison of 2-T and 4-T perovskite/CIGS T-SCs, highlighting key differences in design, performance, and adaptability

Aspect	2-T	4-T
Efficiency potential	Higher efficiency from the series connection and spectral overlap	Lower efficiency due to the independent operation of sub-cells
Current matching	Requires current matching between sub-cells	No current matching needed, allows flexibility in sub-cell optimization
Manufacturing complexity	Simpler due to fewer electrical contacts and lower wiring complexity	More complex due to additional electrical connections
System complexity	Simple system with a single output	More complex, requiring separate outputs for sub-cells
Design flexibility	Simple system with a single output	Greater flexibility in material choice for sub-cell optimization
Cost	Lower due to simpler structure and reduced components	Higher due to added system integration and packaging
Spectral efficiency	Optimized for complementary spectral absorption	Separate optimization, leading to potential losses in efficiency
Flexibility in material choice	Limited by the need for matched bandgaps	Higher flexibility for tailored optimizations
Interconnection losses	Fewer losses, both sub-cells share output	More losses due to separate electrical circuits
Commercialization potential	High potential due to lower cost and simpler manufacturing	Challenging due to added complexity and potential conversion losses

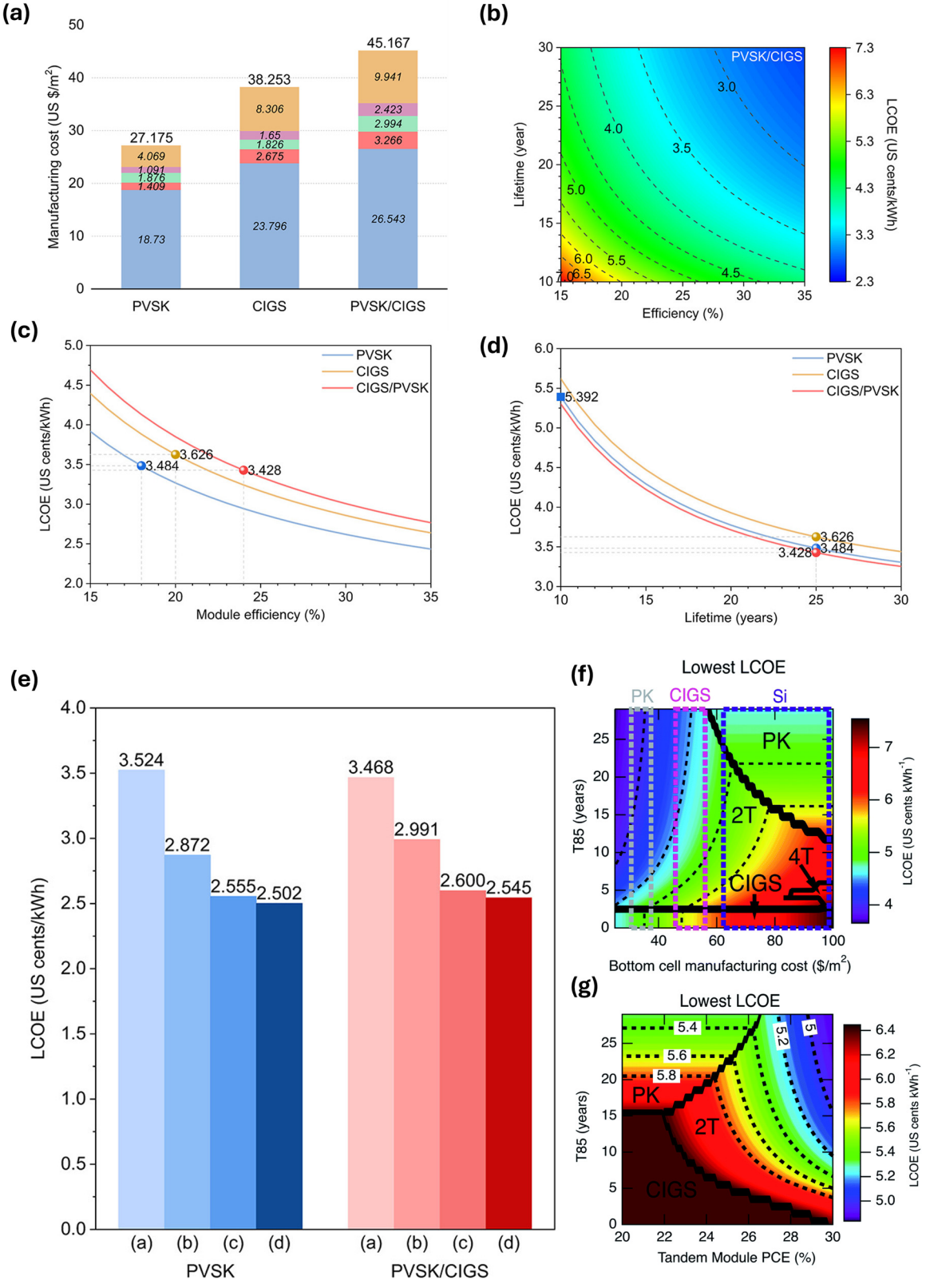

Figure 6: (a) Comparison of manufacturing costs of perovskite (PVSK), CIGS, and 2-T T-SCs (PVSK/CIGS). (b) Combined effect of device efficiency and lifetime on the LCOE for 2-T T-SCs. Independent effect of (c) efficiency and (d) lifetime on LCOE for perovskite, CIGS, and 2-T T-SCs. (e) Calculated LCOE for the PV system with a 30-year lifetime, comparing scenarios with and without device replacement under various assumptions. Reproduced with permission from Wang *et al.* [104]. Copyright 2022, American Chemical Society. (f) and (g) LCOE phase diagram with the *y*-axis as top cell lifetime to be the time at which 85% of the initial output could still be generated, and the *x*-axis of (f) bottom cell manufacturing cost and (g) tandem module PCE. The black solid line represents the borders at which technology is preferable. Reproduced under terms of the CC-BY license [105]. Copyright 2022, R. H. Ahangharnejhad *et al.*, Royal Society of Chemistry.

and the 2-T configuration of T-SCs at 45.17 US $/m^2. Notably, while PSCs have the lowest cost, the manufacturing cost of the T-SCs is still significantly lower than the combination cost of separate perovskite and CIGS modules. Figure 6b shows the combined impact of the efficiency and lifetime of T-SCs devices on the LCOE. It is evident that an increase in module efficiency results in a substantial reduction in LCOE, as shown by the exponential relationship between efficiency and LCOE in Figure 6c. With a 24% efficiency, T-SCs achieve an LCOE of 3.426 U.S. cents/kW h, the lowest LCOE at the highest efficiency compared to single-junction perovskite and CIGS. Additionally, the LCOE decreases rapidly within the 10–30-year lifetime range, emphasizing that a longer lifetime significantly lowers the LCOE, as shown in Figure 6d. When compared to CIGS, PSCs exhibit a lower LCOE for the same lifetime, mainly due to their lower manufacturing cost. Notably, the LCOE of T-SCs is even lower (3.428 U.S. cents/kW h in a 25-year lifetime) than that of single-junction PSC, despite the higher manufacturing cost, underscoring the advantages of T-SCs. This reduction in LCOE is attributed to the increased power output without a proportional increase in other system costs, such as BOS, land, support structures, wiring, power conditioning, and installation, which offsets the higher manufacturing cost. This finding suggests that upgrading to T-SCs can be a cost-effective strategy within existing production frameworks.

This cost-effectiveness highlights the potential for T-SCs to integrate seamlessly into existing PV systems, particularly as they offer a pathway to reducing LCOE over time. However, the long-term economic feasibility of such systems also depends on factors like device replacement and performance over their operational lifespan. Qi Chen *et al.* also investigated whether device replacement remains economically feasible if the anticipated improvements in device cost and performance do not improve as expected. They compared the LCOE for a PV system with a 30-year lifetime under various replacing scenarios: (a) no device replacement; (b) device replacement after 15 years, assuming that the new device's efficiency, cost, and degradation rate are the same as those at year 0; (c) device replacement after 15 years, assuming that the new device's efficiency and cost are based on year 15, while the degradation rate is still based on year 0; and (d) device replacement after 15 years, assuming that the new device's efficiency, cost, and degradation rate are based on year 15. As shown in Figure 6e, the LCOE for a perovskite device with device replacement remains highly competitive, even under the assumption of constant device cost and performance. If research and development lead to improvements in device efficiency and reductions in fabrication costs, the LCOE with replacement could decrease to approximately 70% of the value without replacement. This analysis highlights that module replacement could significantly enhance the competitiveness of emerging PV technologies, such as perovskites, particularly with future advancements in efficiency and cost reductions.

In a different study, the researchers explore the impact of the cost of the bottom cell influences the LCOE, varying the bottom cell cost while keeping its optical and electrical properties constant. The minimum sustainable prices for both 2-T and 4-T configurations were calculated, and the LCOE was assessed for 30-year deployment period in Phoenix, AZ [105]. The study, depicted in Figure 6f, examined the relationship between the perovskite submodule of 85% of its initial performance after degradation (T85) and the manufacturing cost of the bottom cell. The findings revealed that a 2-T tandem module is more cost-effective and has the highest potential for market success, provided that the bottom cell manufacturing cost does not exceed 58 US$/m^2 and T85 above 3 years. Furthermore, the study found that combining perovskite with CIGS is a more cost-effective option compared to pairing perovskite with crystalline silicon (c-Si), as the manufacturing cost of perovskite/CIGS is estimated to be between 34.2 and 50.9 US $/m^2, which is significantly lower than the cost of Si-based devices, which range from 68.3 US$/m^2 to 89.6 US$/m^2. As shown in Figure 6g, a 2-T configuration with PCE above 27% and a T85 3 years results in a lower LCOE compared to single-junction modules.

Another key indicator of sustainability for T-SCs is the EPBT and EROI. EPBT refers to the period required for a PV system to generate enough energy to offset the energy used in its production. EROI, on the other hand, is a dimensionless ratio that compares the total energy produced by the system over its lifetime to the energy required for its manufacturing. EPBT should be low, meaning the PV system should take as little time as possible to generate the amount of energy required to produce it. EROI should be high, meaning the system should produce significantly more energy over its lifetime than was required for its manufacture. The calculations for EPBT and EROI are shown in equations (3)–(5):

$$\mathrm{EPBT(year)} = \frac{E_{\mathrm{in}}}{E_{\mathrm{out}}}, \tag{3}$$

where

$$E_{\mathrm{out}} = I \times \mathrm{PCE} \times PR \times \varepsilon, \tag{4}$$

$$\mathrm{EROI} = \frac{\mathrm{Lifetime}}{\mathrm{EPBT}}. \tag{5}$$

Here, E_{in} represents the primary energy demand (MJ m^{-2}) and E_{out} denotes the annual energy generated (MJ m^{-2} year^{-1}), I is the solar insolation constant (kW h/m^2 year),

PR refers to the performance ratio (PR) of the actual to theoretical energy output module (%), and ε is the energy-to-electricity conversion efficiency factor.

Celik *et al.* investigated the EPBT and EROI of perovskite top cells when paired with different bottom cells, including CIGS and Si [106]. Using a solar insolation constant of 1,700 kW h m^{-2} $year^{-1}$ for Southern Europe, and assuming a PCE of 19.5% for the 2-T PSC/CIGS, along with a uniform PR of 75%, the EPBT for the CIGS bottom device was found to be 5.6 months, while the 2-T perovskite/CIGS configuration had an EPBT of 6.4 months. In comparison, the EPBT for the Si bottom device and the 2-T Si/perovskite tandem were 9.4 and 11.6 months, respectively. The longer EPBT of the 2-T devices compared to single-junction cells is expected, as the perovskite tandem field is still evolving, and current PCEs remain relatively low. Nevertheless, the 2-T perovskite/CIGS configuration outperforms the perovskite/Si T-SC in terms of EPBT. In terms of EROI, the 2-T perovskite/CIGS configuration exhibits better performance. With a PCE of 19.5%, the EROI for the perovskite/CIGS tandem after 5 years of operation was 9.2, compared to 5.2 for the Si/perovskite tandem with a PCE of 21% over the same period.

4.2 Environmental impact

The environmental perspective of T-SCs is complex, considering both the ecological footprint of raw materials and the implications of their deployment. The production of Si involves the extraction of Si, while CIGS involves the extraction of In and Ga. Although these materials are relatively abundant, their extraction may pose environmental risks due to mining practices. Conversely, perovskite materials often utilize a solution-based process, reducing the environmental burden associated with sourcing. However, the potential for toxic metal content in certain perovskite formulations, particularly lead, raises valid concerns regarding environmental safety. Ongoing research is focused on developing lead-free alternatives and encapsulation strategies that mitigate the risks of leaching.

Given these environmental concerns, it is crucial to evaluate the overall impact of T-SCs compared to other solar technologies. Celik *et al.* evaluated the environmental effects of various perovskite-based tandem devices, comparing them to single-junction c-Si solar cells [107]. Their analysis concluded that producing a single 2-T device is a more environmentally sustainable option than manufacturing two separate 4-T single-junction cells. This approach can lead to a 30% reduction in environmental impact, primarily by eliminating the need for additional glass, encapsulation, and front and back contact layers.

Figure 7 illustrates the impact of integrating perovskite into the Si and CIGS bottom cells. Figure 7a presents the environmental impact across various categories, showing the normalized environmental impacts of single-junction PV technologies compared to integrated 2-T tandem configurations on a per-unit area (m^2) basis. The reference case of silicon is represented in yellow, indicating a neutral environmental impact. When comparing the tandem of perovskite and silicon to perovskite and CIGS, the latter proves to be more environmentally preferable, except in the case of acidification. Acidification is primarily attributed to the use of *N*,*N*-dimethylformamide in the fabrication of the lead-based perovskite active layer. However, the acidification impact for the Si/perovskite tandem is notably worse [108]. On average, the environmental impacts of the 2-T configuration with perovskite and CIGS are lower (0.73 m^2) than those of the perovskite and Si tandem (1.22 m^2).

Figure 7b shows the sensitivity of the kW h-based impacts to PCE and lifetime by converting impacts from per m^2 to per kW h using equation (6). In this equation, impacts_{m^2} represents the impact per 1 m^2 of the module area during manufacturing, while $\text{impacts}_{\text{kW h}}$ refers to the impact per kW h of energy generation by the PV module. The equation also incorporates solar insolation (I), solar insolation constant (kW h m^{-2} $year^{-1}$), PR of the module (PR, %), and technology lifetime (Lt, year).

$$\text{Impacts}_{\text{kW h}} = \frac{\text{Impacts}_{m^2}}{I \times \text{PCE} \times \text{PR} \times \text{Lt}}. \tag{6}$$

Higher values of $\text{impacts}_{\text{kW h}}$ suggest that the panel does not produce substantial power. According to the calculation, the 2-T configuration of CIGS and perovskite generates more power than the Si and perovskite tandem.

Figure 7c and d shows the impact per kW h of PCE and lifetime assumptions on the normalized average environmental impacts of tandem cells. In both figures, the diamonds, which represent the impact corresponding to the current lifetime and PCE of the 2-T tandem, show no significant differences. In comparison to Figure 7c, for the CIGS and perovskite tandem with a 15-year lifetime and a device PCE of 30%, this configuration achieves a neutral environment preference, whereas the Si and perovskite tandem, at the same PCE and lifetime level, remains among the least environmentally preferable options.

5 Overview of critical layers in 2-T configurations

Based on environmental and cost analyses, the development of 2-T configurations shows considerable potential

for T-SCs. This section will address the key challenges and essential layers required for the successful realization of 2-T configuration cells. As illustrated in Figure 5a and Figure 8, the 2-T structure comprises several critical layers. Starting from the CIGS sub-cell located at the bottom of the device architecture, the structure typically includes a substrate (usually glass or plastic), followed by a back electrode, commonly molybdenum. Above this is the CIGS absorption layer, followed by the buffer layer, commonly CdS, and the window layer of intrinsic ZnO (i-ZnO) and aluminum-doped ZnO (AZO). For the top perovskite

(a)

	PV technology	CIGS/PK_{Pb}	CIGS	Si/PK_{Pb}	Si	Si [m^2]
Impact Categories	Acidification	1.22	0.66	1.68	1	5.39E-01 [kg SO_2-Equiv.]
	Ecotoxicity	1.02	0.97	1.19	1	7.28E+02 [CTU_e]
	Eutrophication	0.97	0.77	1.36	1	7.13E-01 [kg N-Equiv.]
	Global warming	0.52	0.49	1.13	1	1.49E+02 [kg CO_2-Equiv.]
	Human health particulate	0.66	0.60	1.15	1	8.63E-02 [kg $PM_{2.5}$-Equiv.]
	Human toxicity, cancer	0.56	0.52	1.14	1	1.09E-05 [CTU_h]
	Human toxicity, non-cancer	1.14	1.10	1.26	1	3.68E-05 [CTU_h]
	Ozone depletion	0.30	0.27	1.08	1	1.75E-05 [kg CFC 11-Equiv.]
	Resources	0.34	0.31	1.08	1	1.98E+02 [MJ surplus energy]
	Smog formation	0.53	0.50	1.12	1	6.86E+00 [kg O_3-Equiv]
Average	Bottom (Impacts/m^2)		0.62		1.00	
	PK_{Pb}+ TJ (Impacts/m^2)	0.11		0.22		
	Tandem (Impacts/m^2)	0.73		1.22		

Most environmentally preferable	0.54<
More environmentally preferable	0.55-0.85
Neutral	0.86 - 1.14
Less environmentally preferable	1.15-1.44
Least environmentally preferable	1.45>

(b)

PV technology	CIGS/PK_{Pb}	CIGS	Si/PK_{Pb}	Si
PCE	19.5%	22.3%	21.0%	25.0%
Lt	5	30	5	30
Bottom (Impacts/kWh)		0.69		1.00
Tandem (Impacts/kWh)	5.58		8.71	

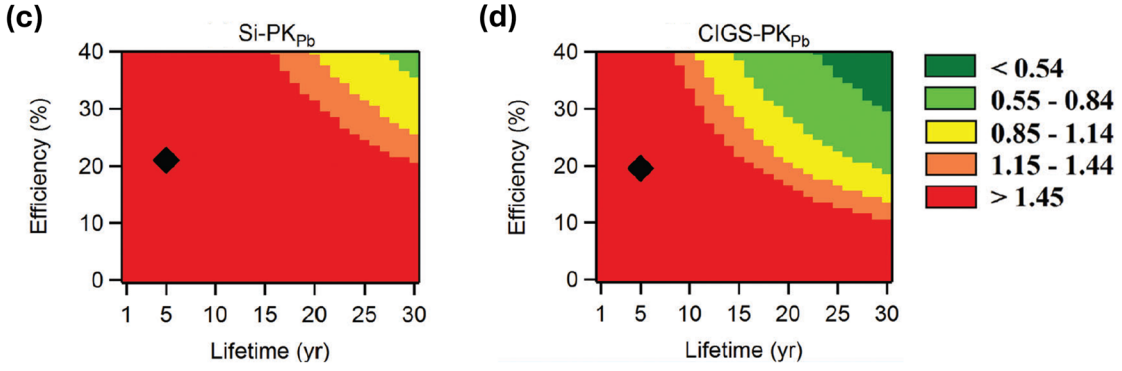

Figure 7: (a) A comparison of the normalized environment impact of single-junction PV *versus* integrated 2-T tandem technologies on a per-unit area (m^2) production basis. The environmental effects of the bottom cell, the tandem configuration, and the difference (difference = PKpb + TJ) between the bottom and the tandem cells are represented in the last three rows. The actual environmental impact values for Si are shown in the rightmost column. (b) A comparison of the normalized environment impact of single-junction PV *versus* integrated 2-T tandem technologies on a per-unit energy (kW h) generation basis. (c) and (d) The influence of PCE and Lt assumptions on the normalized average environmental impacts of tandem cells illustrates how variations in Lt and PCE would impact the environmental effects per kW h. The impacts associated with the current Lt and PCE of the tandems are represented by diamonds. Yellow color indicates that the impact is similar to that of reference Si; values colored in bright and dark green signify better performance, and orange and red indicate poorer performance. Abbreviations: PKpb: perovskite lead, TJ: tunnel junction, Lt: lifetime. Reproduced with permission from Celik *et al.* [107]. Copyright 2017, Royal Society of Chemistry.

sub-cell, from the top, the structure features a transparent electrode, typically ITO, which allows sunlight to penetrate the cell. The light then passes through the ETL, which may include materials like BCP and ZnO, and further through a layer of PCBM and C_{60}, which enhance electron mobility. Beneath the ETL is the absorption layer for the top cell, which consists of a perovskite active material, followed by an HTL such as PEDOT:PSS and PTAA. The integration of the top and bottom cells in a device is highly dependent on the interconnection layer, which plays a critical role in determining the overall device performance. Poor contact at the interconnection can lead to increased series resistance (R_s), resulting in a significant reduction up to 60% in the fill factor (FF) of the entire 2-T device. Additionally, selecting an appropriate window layer for the CIGS is essential, as the typical i-ZnO and AZO layers in conventional CIGS consist of ZnO, which can degrade the perovskite layer. However, removing these layers compromises the original CIGS device architecture, ultimately leading to a decline in its performance [86]. Rough CIGS morphology is also another challenging factor. Its typical roughness ranges from 50 to 200 nm, with features between 500 nm and 1 µm, depending on the processing. Because of this, applying a perovskite top cell with thin selective contacts, which is the most common and efficient method, is difficult and often leads to shunting in the tandem device [87].

5.1 HTL of PSC

To prevent potential shunting in 2-T T-SCs caused by the rough surface of the CIGS layer, Jošt *et al.* employed ALD to conformally deposit a thin NiO_x layer on the front contact of the CIGS bottom cell. A PTAA film was then spin-coated on top of the NiO_x layer to form a bilayer p-type contact, referred to as the double HTL. The cross-sectional scanning transmission electron microscopy (STEM) image and the energy-dispersive X-ray (EDX) analysis of the Zn and Ni material composition are shown in Figure 9a. The 10 nm NiO_x layer effectively smoothened the surface of the rough 150 nm ZnO layer, preventing direct contact between the perovskite and ZnO:Al. As shown in Figure 9b, this configuration achieved an impressive PCE of 21.6% by incorporating the NiO_x/PTAA double HTL. Notably, the device demonstrated exceptional stability, maintaining MPP tracking over a 10-min period on an active area of 0.778 cm^2.

To improve upon the NiO_x layer by using ALD and the current HTL of PTAA, a subsequent study by the same group synthesized new self-assembled monolayers (SAMs), including (2-(3,6-bis[bis(4-methoxyphenyl)amino]-9H-carbazol-9-yl)ethyl)phosphonic acid, V1036 [2-(3,6-dimethoxy-9H-carbazol-9-yl)ethyl]phosphonic acid, MeO-2PACz, and [2-(9H-carbazol-9-yl)ethyl]phosphonic acid, 2PACz (Figure 9c). These SAMs enable a simple process, where the CIGS is dipped into the SAM solution, creating hole-selective contacts with minimized non-radiative losses, making them suitable for manufacturing on rough CIGS surfaces. Among these, MeO-2PACz outperforms both PTAA and V1036 due to its reduced absorption in the visible spectrum, a shorter reaction scheme, and the absence of metal-based catalysts, making it a more cost-effective alternative. Figure 9d shows the *J–V* curve of the device,

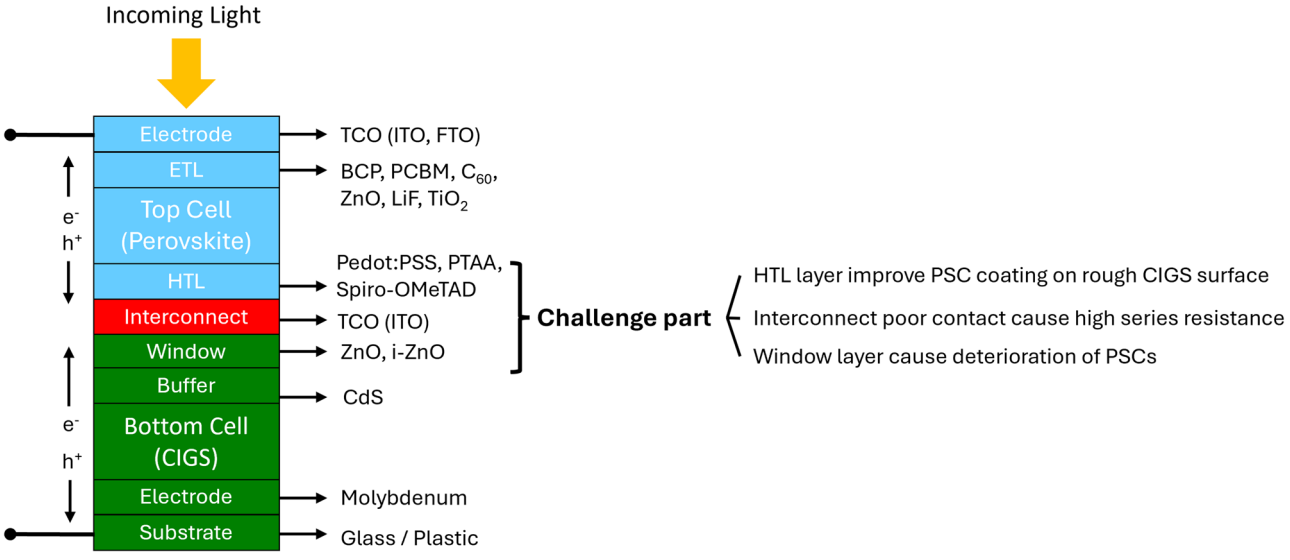

Figure 8: Schematic of 2-T T-SC devices with example of materials used in each layer.

achieving 23.26% PCE on an active area of 1.03 cm^2, along with an SEM image of the cross-sectional view of the 2-T device using the MeO-2PACz HTL.

Building on these advances with SAMs and HTL. Kafedjiska *et al.* investigated 2-T T-SCs with three different HTLs (NiO_x + SAM, NiO_x:Cu + SAM, and SAM only) [89]. SAM consists of MeO-2PACz and NiO_x:Cu is 2 wt% copper-doped NiO_2, and the device structure is shown in Figure 9e. Their best PCE of 23.2% was found with rapid-thermal processing (RTP) CIGS-based bottom sub-cell and the HTL of NiO_x:Cu + SAM. Figure 9f shows the photoluminescence (PL) and dark lock-in thermography (DLIT) images of 2-T T-SCs with different HTLs. NiO_x:Cu + SAM can act as a promising shunt-quenching layer below the SAM layer.

Boukortt *et al.* conducted a numerical analysis of 2-T T-SCs using Silvaco TCAD tools [109]. They varied the thickness of the Spiro-OMeTAD and p-doped Spiro-OMeTAD HTL from 0 to 200 nm to determine the optimal values for

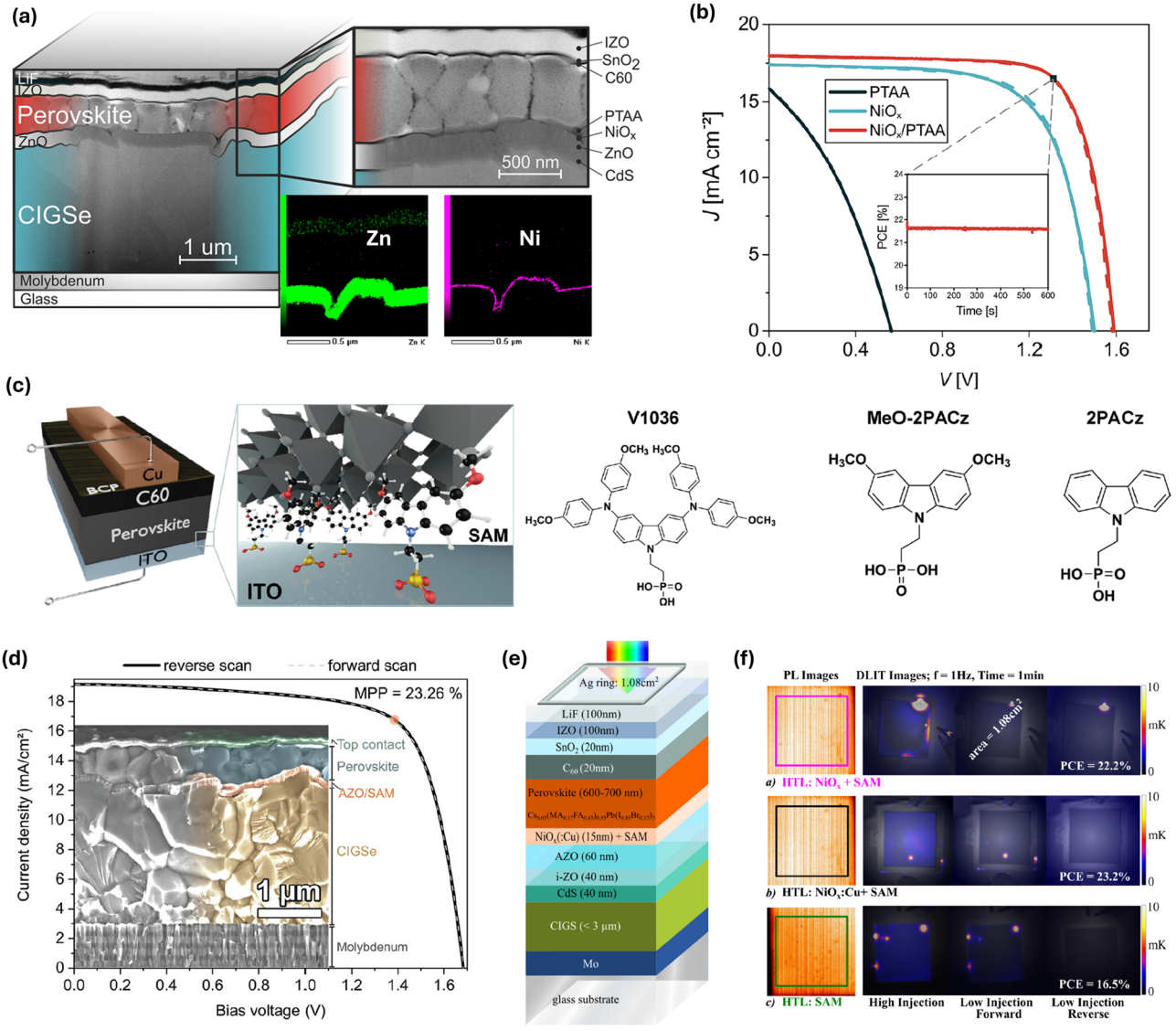

Figure 9: (a) STEM cross-sectional image of 2-T T-SCs with EDX analysis of the Zn and Ni material composition. (b) *J–V* characteristic of 2-T T-SCS devices with different HTL layers (PTAA, NiO_x, and double NiO_x/PTAA). The solid line represents the forward scan, while the dashed line shows the reverse scan. The inset displays MPP tracking over 10 min. Reproduced with permission from Jošt *et al.* [87]. Copyright 2019, American Chemical Society. (c) Schematic diagram of the perovskite sub-cell layer with the zoom-in of SAM molecules attached to the ITO surface and the chemical structures of PTAA and SAM molecules (V1036, MeO-2PACz, and 2PACz). (d) *J–V* characteristic and SEM image of the cross-section of 2-T T-SCS devices with the MeO-2PACz HTL layer. The orange circle marks the MPP at 23.26% PCE. Reproduced under terms of the CC-BY license [88]. Copyright 2019. Al-ashouri *et al.*, Royal Society of Chemistry. (e) Device structure of 2-T T-SCs and (f) PL and DLIT images of 2-T T-SCs with different HTLs (NiO_x + SAM, NiO_x:Cu + SAM, and SAM only). Reproduced with permission from Kafedjiska *et al.* [89]. Copyright 2023, published by Elsevier.

perovskite and tandem cells. Their results revealed a significant influence of HTL thickness on the cell performance, as it affects key parameters such as the recombination rate, series resistance, and shunt resistance. Notably, excessive p-type doping in the HTL layer led to reduced hole transport and an increase in recombination rates. The highest efficiency for the T-SCs was achieved with an HTL thickness of 25 nm, resulting in an efficiency improvement to 29%.

5.2 Interconnecting layer (ICL)

The ICL plays a critical role in T-SC architectures by facilitating efficient charge transfer between the top and bottom sub-cells. In CIGS-based T-SCs, the ICL serves as a recombination zone, where electrons from one sub-cell recombine with holes from the adjacent sub-cell, effectively linking the two cells in series. Beyond enabling electrical connectivity, the ICL must also provide optical transparency to minimize losses and promote optimal light transmission to the bottom cell. Additionally, ensuring a smooth surface is essential for preventing shunting pathways and ensuring high-quality deposition of subsequent layers. An effective ICL in CIGS-based tandems enhances overall device performance by optimizing electrical, optical, and morphological properties, making it a crucial component in the development of high-efficiency tandem devices.

Han *et al.* worked on smoothing the ICL by enhancing three key aspects of the bottom CIGS sub-cell and achieved an impressive PCE of 22.43% 2-T T-SCs [86]. First, they replaced the traditional metal electrode with a 100 nm ITO layer as the top contact, significantly improving light transmission and ensuring better light penetration. The use of a boron-doped ZnO (BZO) top layer often results in high surface roughness that leads to electrical shorting

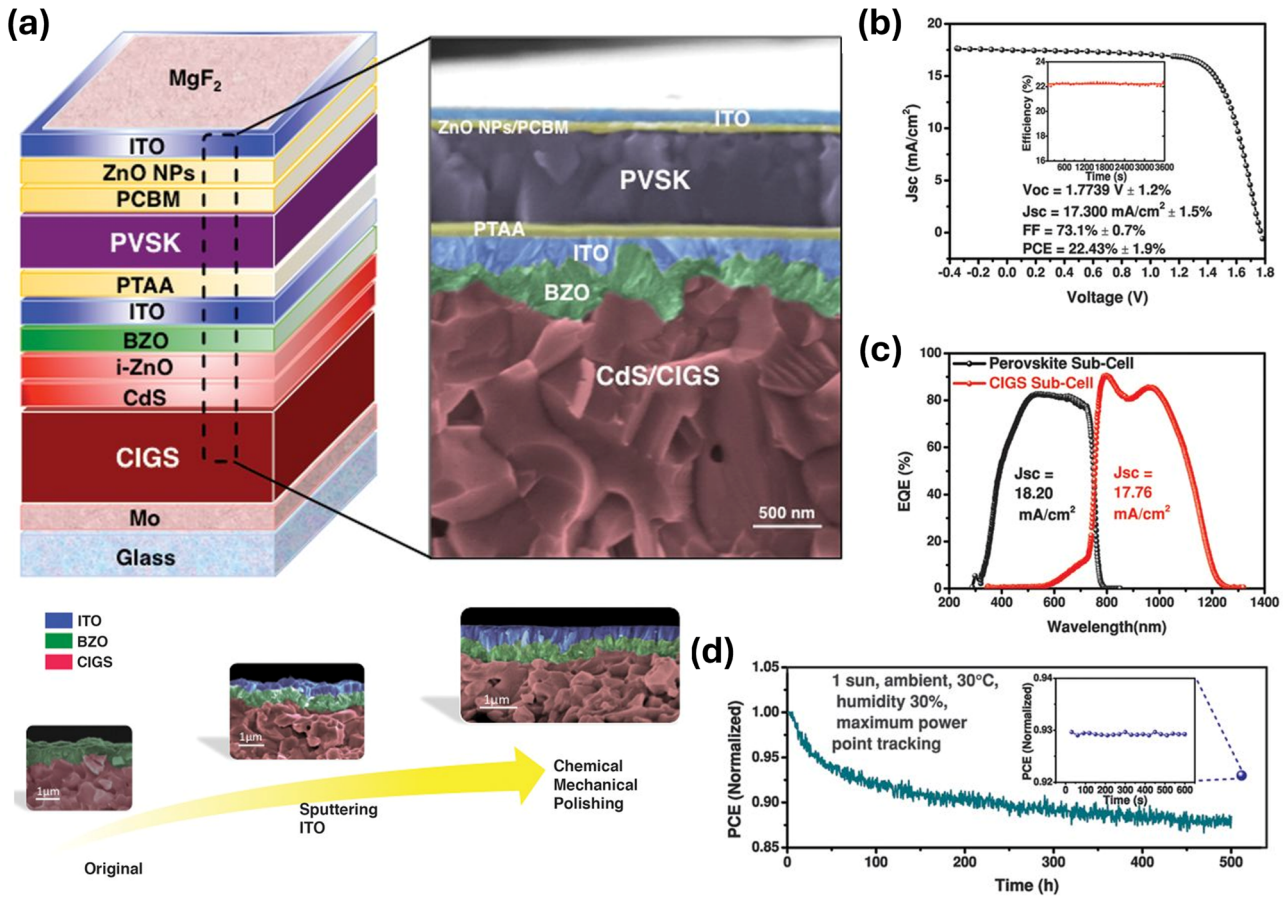

Figure 10: (a) Schematic diagram and cross-sectional SEM image of 2-T perovskite/CIGS T-SCs. (b) NREL-certified *J–V* curve, with an inset showing the PCE at the MPP. (c) EQE spectra for perovskite and the CIGS sub-cell. (d) Stability test of unencapsulated T-SCs for 500 h at 30°C, with an inset displaying the PCE after a 12-h resting period without load and illumination. Reproduced under terms of the CC-BY license [86]. Copyright 2018, Han *et al.*, American Association for the Advancement of Science.

between the top sub-cell and itself. To address this issue, an additional ITO layer, treated with chemical mechanical polishing (CMP), was deposited to smooth the surface and act as an interconnection layer, eliminating the need for a tunneling junction (TJ) between the sub-cells. Finally, a 50 nm 4-isopropyl-4′-methyldiphenyliodonium tetrakis (pentafluorophenyl) borate (TPFB)-doped PTAA layer was precisely applied as the HTL to the perovskite sub-cell (Figure 10a). This approach not only preserved the V_{OC} but also enhanced both the FF and J_{SC}. The device maintained 88% of its initial PCE after 500 h of aging at 30°C under MPP tracking, with 93% of the PCE recoverable after resting for 12 h without load. A comprehensive performance analysis of the tandem cells is shown in Figure 10b–d.

5.3 Other layers

Zhao *et al.* studied the theoretical analysis by studying three key aspects and obtained a PCE of 31.13% with the structure of FTO/TiO_2/$CH_3NH_3PbI_2Br$/Spiro-OMeTAD/ITO/CdS/CIGS/Mo [110]. First, the thickness of perovskite and CIGS is tuned to meet current matching. With the increase of both photoactive layer thickness, the matched current increased due to the increase of photon absorption and then tended to saturation (Figure 11a). Second, reducing the thickness of the top electrode of the perovskite sub-cell, FTO, to improve the optical absorption by minimizing reflection (Figure 11b), and finally, V_{OC} can be increased by increasing the doping concentration of CIGS from 10^{15} to 10^{18} cm^3 (Figure 11c).

Jošt *et al.* with their group optimized the usage of SAM as the HTL [88]. Here, they used the SAM structure of MeO-4PACz as the HTL. The 2-T T-SCs were improvised with PEAI as an additive in the perovskite active layer solution, followed by evaporation of 1 nm LiF, 20 nm C_{60}, ALD of 20 nm SnO_2, sputtering 95 nm IZO as TCO, and evaporation of 110 nm LiF as an antireflecting coating, as shown by the cross-sectional SEM in Figure 11d [5]. The device exhibited excellent performance with a stabilized MPP of 24.2%, certified by Fraunhofer ISE, as shown in Figure 11e. The main improvement lies in an increased V_{OC} of 1.77 V due to the higher perovskite bandgap of 1.68 eV, Me-4PACz HTL, PEAI additive, and LiF interlayer. Figure 11f shows the EQE and reflection spectra; a reflection loss of 2.2 mA cm^{-2} was found due to the rough surface of the CIGS absorber, which results in excellent antireflection properties and enables high optical potential of perovskite/CIGS devices with little

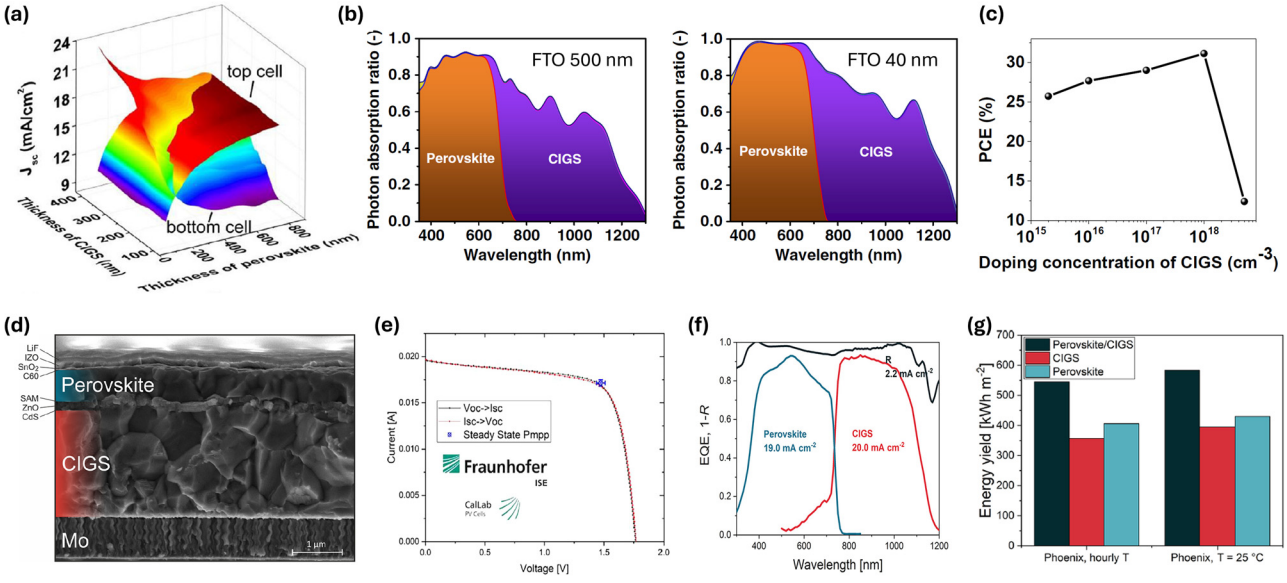

Figure 11: (a) Current matching of 2-T T-SCS with different thicknesses of CIGS and $CH_3NH_3PbI_2Br$ halide compositions, (b) photon absorption with 500 nm (left) and 40 nm (right) of FTO layer thickness, and (c) PCE of 2-T T-SCs with different doping concentrations. Reproduced with permission from Zhao *et al.* [110]. Copyright 2019, John Wiley and Sons. (d) Cross-sectional SEM image of 2-T T-SCs with SAM/ZnO/CdS as the HTL, window, and buffer layer. (e) Certified *I*–*V* characteristics and (f) EQE and 1-R spectra of the fabricated 2-T T-SCs. (g) Energy yield of single-junction CIGS and perovskite as compared to 2-T T-SCS. Bars on the left show the case where hourly temperatures (daily profiles) were considered, while the bars on the right show results where the temperature was fixed at 25°C. Reproduced under terms of the CC-BY license [5]. Copyright 2022, Jošt *et al.*, American Chemical Society.

parasitic absorption in the device. Figure 11g shows energy yield results of the three analyzed technologies for Phoenix, Arizona, where a hot climate should show the largest difference. The perovskite/CIGS tandem significantly outperforms both subcell standalone technologies by more than 30 and 50% in the cases of perovskite and CIGS, respectively.

6 Future direction

As T-SCs continue to push the boundaries of efficiency, material innovation, and economic feasibility, future research in this domain is expected to explore several key directions to further improve their performance and scalability:

Advanced light management techniques: The role of light management in T-SCs, especially those based on perovskite and CIGS, is still an area of active research [111,112]. Novel approaches to light trapping and scattering could significantly enhance the absorption and utilization of light in the active layers. Techniques like plasmonics, nanostructures, and holographic optical elements could be developed to increase the amount of light absorbed by the cells, particularly under low-light conditions. These techniques could potentially be incorporated into the fabrication process without significantly increasing the costs.

Artificial intelligence (AI) in device optimization and material discovery: AI through machine learning techniques holds a lot of potential in accelerating the development of perovskite/CIGS T-SCs. AI can be used to optimize device configurations, predict material properties, and accelerate the discovery of new perovskite compositions with enhanced efficiency. Additionally, AI-driven simulations and models can help identify the most promising fabrication processes, reducing the time and cost associated with trial-and-error experiments [113,114]. As AI continues to evolve, its integration into the design and manufacturing of T-SCs will likely streamline innovation, pushing the boundaries of performance and scalability in the pursuit of cost-effective, high-efficiency solar technologies.

T-SCs for semi-transparent and colorful applications: Semi-transparent and colorful solar cells are gaining attention for their potential in building-integrated PVs and other visually demanding applications [115–118]. Semi-transparent designs can be especially valuable for applications, such as windows, skylights, and facades, where light transmission is required alongside energy generation. Colorful panels, on the other hand, offer aesthetic benefits and can be used in architectural facades, consumer electronics, and automotive surfaces where visual integration is important [119–121]. However, both semi-transparent and colorful T-SCs remain relatively underexplored. Future research could focus on tailoring the optical properties of the perovskite top cell, using advanced light-filtering layers, photonic structures, or composition tuning, to achieve the desired transparency or coloration while maintaining high PCE.

7 Conclusion

In conclusion, the recent developments in perovskite-CIGS T-SCs highlight their significant potential to reshape the PV landscape. By combining the high efficiency of perovskite materials with the established advantages of CIGS technology, these tandem cells can achieve high efficiencies, positioning them as a leading solution in solar energy generation. The 2-T perovskite/CIGS T-SC configuration represents a significant advancement in PV technology. By effectively combining the advantages of both materials and optimizing device structure, researchers are paving the way for higher efficiency solar cells that can be integrated into a variety of applications. As research continues to refine the materials and processes involved, the commercial viability of these tandem devices is expected to increase, contributing to the growing demand for efficient and sustainable energy solutions.

Looking ahead, ongoing research must focus on addressing the challenges related to stability, material toxicity, and scalability. Advancements in encapsulation techniques and the exploration of lead-free perovskite alternatives are essential to ensure long-term commercial viability and environmental safety. Additionally, optimizing manufacturing processes will be crucial to reduce costs and facilitate widespread adoption.

As the demand for renewable energy solutions grows, perovskite/CIGS T-SCs could play a pivotal role in achieving global sustainability goals. Collaborative efforts among researchers, industry stakeholders, and policymakers will be essential to accelerate the commercialization of these technologies. Ultimately, continued innovation in this field promises to enhance energy efficiency and contribute to a more sustainable future, making solar energy a cornerstone of the global energy landscape.

Acknowledgments: S.S. gratefully acknowledges primary financial support from the Geran Galakan Penyelidik Muda (GGPM), grant number GGPM-2023-048, funded by

Universiti Kebangsaan Malaysia. L.X. acknowledges support from the National Natural Science Foundation of China (22209144), the Project of Natural Science Foundation of Yunnan, and Yunnan Revitalization Talent Support Program (202201AU070030 and 202201AT070114). J.X.Z. acknowledges support from the Yunnan University's Research Innovation Fund for Graduate Students (KC-24249796) and Scientific Research Fund of the Education Department of Yunnan Province (2025Y0038).

Funding information: This manuscript was funded by the Geran Galakan Penyelidik Muda (GGPM), Universiti Kebangsaan Malaysia, under grant number GGPM-2023-048.

Author contribution: J.X.Z.: formal analysis, investigation, and writing – original draft. X.L: conceptualization, validation, writing – review and editing, and supervision. S.S: conceptualization, validation, formal analysis, investigation, writing – original draft, writing – review and editing, visualization, supervision, project administration, and funding acquisition. All authors have accepted responsibility for the entire content of this manuscript and approved its submission.

Conflict of interest: The authors state no conflict of interest.

Data availability statement: All data generated or analyzed during this study are included in this published article.

References

[1] Victoria M, Haegel N, Peters IM, Sinton R, Jäger-Waldau A, del Canizo C, et al. Solar photovoltaics is ready to power a sustainable future. Joule. 2021;5(5):1041–56.

[2] Wang R, Huang T, Xue J, Tong J, Zhu K, Yang Y. Prospects for metal halide perovskite-based tandem solar cells. Nat Photonics. 2021;15(6):411–25.

[3] Ramadan AJ, Oliver RD, Johnston MB, Snaith HJ. Methylammonium-free wide-bandgap metal halide perovskites for tandem photovoltaics. Nat Rev Mater. 2023;8(12):822–38.

[4] Duan L, Walter D, Chang N, Bullock J, Kang D, Phang SP, et al. Stability challenges for the commercialization of perovskite–silicon tandem solar cells. Nat Rev Mater. 2023;8(4):261–81.

[5] Jost M, Köhnen E, Al-Ashouri A, Bertram T, Tomšič SP, Magomedov A, et al. Perovskite/CIGS tandem solar cells: from certified 24.2% toward 30% and beyond. ACS Energy Lett. 2022;7(4):1298–307.

[6] Liang H, Feng J, Rodríguez-Gallegos CD, Krause M, Wang X, Alvianto E, et al. 29.9%-efficient, commercially viable perovskite/CuInSe2 thin-film tandem solar cells. Joule. 2023;7(12):2859–72.

[7] Siegler TD, Shimpi TM, Sampath WS, Korgel BA. Development of wide bandgap perovskites for next-generation low-cost CdTe tandem solar cells. Chem Eng Sci. 2019;199:388–97.

[8] Brinkmann KO, Wang P, Lang F, Li W, Guo X, Zimmermann F, et al. Perovskite–organic tandem solar cells. Nat Rev Mater. 2024;9(3):202–17.

[9] Park J, Kim J, Yun H-S, Paik MJ, Noh E, Mun HJ, et al. Controlled growth of perovskite layers with volatile alkylammonium chlorides. Nature. 2023;616(7958):724–30.

[10] Jeong MJ, Moon CS, Lee S, Im JM, Woo MY, Lee JH, et al. Boosting radiation of stacked halide layer for perovskite solar cells with efficiency over 25%. Joule. 2023;7(1):112–27.

[11] Huang Z, Bai Y, Huang X, Li J, Wu Y, Chen Y, et al. Anion–π interactions suppress phase impurities in FAPbI3 solar cells. Nature. 2023;623(7987):531–7.

[12] Liang Z, Zhang Y, Xu H, Chen W, Liu B, Zhang J, et al. Homogenizing out-of-plane cation composition in perovskite solar cells. Nature. 2023;624(7992):557–63.

[13] Zheng Y, Li Y, Zhuang R, Wu X, Tian C, Sun A, et al. Towards 26% efficiency in inverted perovskite solar cells via interfacial flipped band bending and suppressed deep-level traps. Energy Environ Sci. 2024;17(3):1153–62.

[14] Chen H, Liu C, Xu J, Maxwell A, Zhou W, Yang Y, et al. Improved charge extraction in inverted perovskite solar cells with dual-site-binding ligands. Science. 2024;384(6692):189–93.

[15] Zhou J, Tan L, Liu Y, Li H, Liu X, Li M, et al. Highly efficient and stable perovskite solar cells via a multifunctional hole transporting material. Joule. 2024;8(6):P1691–706.

[16] Li X, Gao S, Wu X, Liu Q, Zhu L, Wang C, et al. Bifunctional ligand-induced preferred crystal orientation enables highly efficient perovskite solar cells. Joule. 2024;8(11):P3169–85.

[17] Green MA, Ho-Baillie A, Snaith HJ. The emergence of perovskite solar cells. Nat Photonics. 2014;8(7):506–14.

[18] Qi S, Ge C, Wang P, Wu B, Zhao Y, Zhao R, et al. Improving perovskite solar cell performance and stability via thermal imprinting-assisted ion exchange passivation. ACS Appl Mater Interfaces. 2024;16(38):51037–45.

[19] Zhang X, Wang L, Shafian S, Wang P, Zhao Y, Wang P, et al. Crosslinking-driven chemical homogeneity enhances performance of pre-seeded perovskite solar cells. Small. 2024;21(6):2408362.

[20] Wang P, Shafian S, Qiu F, Zhang X, Zhao Y, Wu B, et al. Improving redox reactions of Spiro-OMeTAD via p-type molecular scaffold to reduce energy loss at Ag-electrode in perovskite solar cells. J Energy Chem. 2025;102:151–60.

[21] Zulhafizhazuan W, Sobayel K, Shafian S, Sepeai S, Ibrahim MA. Preliminary study on planar-mixed dimensional Cs3Bi2I9 solar cells: SCAPS-1D simulation and experimental analysis. Interactions. 2025;246(1):29.

[22] Lee S, Yoon YS, Shafian S, Kim JY, Kim K. Sequential Co-deposition of perovskite film: an effective way of tailoring bandgap in all vacuum processed perovskite solar cells. Small Methods. 2025;2500104. doi: 10.1002/smtd.202500104.

[23] De Wolf S, Holovsky J, Moon S-J, Loper P, Niesen B, Ledinsky M, et al. Organometallic halide perovskites: sharp optical absorption edge and its relation to photovoltaic performance. J Phys Chem Lett. 2014;5(6):1035–9.

[24] Yin W-J, Shi T, Yan Y. Superior photovoltaic properties of lead halide perovskites: insights from first-principles theory. J Phys Chem C. 2015;119(10):5253–64.
[25] Kabi O, Abu-Jafar MS, Farout M, Mousa AA, Bouhemadou A, Erum N, et al. Ab initio investigation of the structural, elastic, dynamic, electronic, and magnetic properties of cubic perovskite CeCrO3. ACS Omega. 2024;9(10):11820–8.
[26] Saliba M, Correa-Baena JP, Grätzel M, Hagfeldt A, Abate A. Perovskite solar cells: from the atomic level to film quality and device performance. Angew Chem, Int Ed. 2018;57(10):2554–69.
[27] Shafian S, Hwang H, Kim K. Near infrared organic photodetector utilizing a double electron blocking layer. Opt Express. 2016;24(22):25308–16.
[28] Ryu KY, Shafian S, Shin J, Lee YJ, Lee M, Kim K. Linear polyurethane ionenes for stable interlayer of organic photovoltaics. J Power Sources. 2022;542:231772.
[29] Shin S, Shafian S, Ryu KY, Jeon YK, Kim WS, Kim K. Solution-processed TiO2 nanoparticles functionalized with catechol derivatives as electron transporting layer materials for organic photovoltaics. Adv Mater Interfaces. 2022;9(14):2200118.
[30] Rajagopal A, Yao K, Jen AKY. Toward perovskite solar cell commercialization: a perspective and research roadmap based on interfacial engineering. Adv Mater. 2018;30(32):1800455.
[31] Chen J, Park N-G. Materials and methods for interface engineering toward stable and efficient perovskite solar cells. ACS Energy Lett. 2020;5(8):2742–86.
[32] Luo D, Yang W, Wang Z, Sadhanala A, Hu Q, Su R, et al. Enhanced photovoltage for inverted planar heterojunction perovskite solar cells. Science. 2018;360(6396):1442–6.
[33] Min H, Lee DY, Kim J, Kim G, Lee KS, Kim J, et al. Perovskite solar cells with atomically coherent interlayers on SnO_2 electrodes. Nature. 2021;598(7881):444–50.
[34] Luo X, Shen Z, Shen Y, Su Z, Gao X, Wang Y, et al. Effective passivation with self-organized molecules for perovskite photovoltaics. Adv Mater. 2022;34(26):2202100.
[35] Li X, Wu X, Li B, Cen Z, Shang Y, Lian W, et al. Modulating the deep-level defects and charge extraction for efficient perovskite solar cells with high fill factor over 86%. Energy Environ Sci. 2022;15(11):4813–22.
[36] Shen Z, Han Q, Luo X, Shen Y, Wang T, Zhang C, et al. Crystal-array-assisted growth of a perovskite absorption layer for efficient and stable solar cells. Energy Environ Sci. 2022;15(3):1078–85.
[37] Deng L, Wang H, Rafique S, Wang Y, Hu T, Liu K, et al. Stabilizing bottom side of perovskite via preburying cesium formate toward efficient and stable solar cells. Adv Funct Mater. 2023;33(43):2303742.
[38] Yang T, Gao L, Lu J, Ma C, Du Y, Wang P, et al. One-stone-for-two-birds strategy to attain beyond 25% perovskite solar cells. Nat Commun. 2023;14(1):839.
[39] Yan L, Huang H, Cui P, Du S, Lan Z, Yang Y, et al. Fabrication of perovskite solar cells in ambient air by blocking perovskite hydration with guanabenz acetate salt. Nat Energy. 2023;8(10):1158–67.
[40] Wang Q, Chen Y, Chen X, Tang W, Qiu W, Xu X, et al. Tailored succinic acid-derived molecular structures toward 25.41%-efficiency and stable perovskite solar cells. Adv Mater. 2024;36(6):2307709.
[41] Zhou J, Lv J, Tan L, Li H, Jiao B, Li M, et al. High-efficiency large-area perovskite solar cells via a multifunctional crystallization regulating passivation additive. Adv Mater. 2025;37(26):2502916.
[42] Jiao B, Tan L, Ye Y, Ren N, Li M, Li H, et al. One-stone-two-birds: over 26% efficiency in perovskite solar cells via synergistic crystallization & interface regulation. Energy Environ Sci. 2025;18:5437–47.
[43] Jiang Q, Tong J, Xian Y, Kerner RA, Dunfield SP, Xiao C, et al. Surface reaction for efficient and stable inverted perovskite solar cells. Nature. 2022;611(7935):278–83.
[44] Zhang S, Ye F, Wang X, Chen R, Zhang H, Zhan L, et al. Minimizing buried interfacial defects for efficient inverted perovskite solar cells. Science. 2023;380(6643):404–9.
[45] Peng W, Mao K, Cai F, Meng H, Zhu Z, Li T, et al. Reducing nonradiative recombination in perovskite solar cells with a porous insulator contact. Science. 2023;379(6633):683–90.
[46] Li Z, Sun X, Zheng X, Li B, Gao D, Zhang S, et al. Stabilized hole-selective layer for high-performance inverted pin perovskite solar cells. Science. 2023;382(6668):284–9.
[47] Yang Y, Chen R, Wu J, Dai Z, Luo C, Fang Z, et al. Bilateral chemical linking at NiO_x buried interface enables efficient and stable inverted perovskite solar cells and modules. Angew Chem, Int Ed. 2024;136(36):e202409689.
[48] Gong C, Li H, Wang H, Zhang C, Zhuang Q, Wang A, et al. Silver coordination-induced n-doping of PCBM for stable and efficient inverted perovskite solar cells. Nat Commun. 2024;15(1):4922.
[49] Zhu Z, Ke B, Sun K, Jing C, Song Z, Jiang R, et al. High-performance inverted perovskite solar cells and modules via aminothiazole passivation. Energy Environ Sci. 2025;18:4120–9.
[50] Xu Z, Sun X, Hui W, Wang Q, Xu P, Tang W, et al. Optimizing molecular packing and interfacial contact via halogenated N-glycidyl carbazole small molecules for low energy loss and highly efficient inverted perovskite solar cells. Angew Chem, Int Ed. 2025;64(26):e202503008.
[51] Saber S, Marí B, Andrio A, Escorihuela J, Khattab N, Eid A, et al. Structural and electrochemical analysis of CIGS: Cr crystalline nanopowders and thin films deposited onto ITO substrates. Nanomaterials. 2021;11(5):1093.
[52] Machkih K, Oubaki R, Makha M. A review of CIGS thin film semiconductor deposition via sputtering and thermal evaporation for solar cell applications. Coatings. 2024;14(9):1088.
[53] Mufti N, Amrillah T, Taufiq A, Diantoro M, Nur H. Review of CIGS-based solar cells manufacturing by structural engineering. Sol Energy. 2020;207:1146–57.
[54] Luque AHS. Handbook of photovoltaic science and engineering. Hoboken, NJ, USA: John Wiley & Sons, Ltd.; 2011.
[55] Wang Y-C, Shieh H-PD. Improvement of bandgap homogeneity in Cu (In, Ga) Se_2 thin films using a modified two-step selenization process. Appl Phys Lett. 2013;103(15):153502.
[56] Chandra A, Anderson G, Melkote S, Gao W, Haitjema H, Wegener K. Role of surfaces and interfaces in solar cell manufacturing. CIRP Ann. 2014;63(2):797–819.
[57] Ramanujam J, Bishop DM, Todorov TK, Gunawan O, Rath J, Nekovei R, et al. Flexible CIGS, CdTe and a-Si: H based thin film solar cells: A review. Prog Mater Sci. 2020;110:100619.
[58] Ramanujam J, Singh UP. Copper indium gallium selenide based solar cells–a review. Energy Environ Sci. 2017;10(6):1306–19.
[59] Ghorbani E, Kiss J, Mirhosseini H, Roma G, Schmidt M, Windeln J, et al. Hybrid-functional calculations on the incorporation of Na and K impurities into the CuInSe2 and CuIn5Se8 solar-cell materials. J Phys Chem C. 2015;119(45):25197–203.
[60] Jackson P, Hariskos D, Lotter E, Paetel S, Wuerz R, Menner R, et al. New world record efficiency for Cu (In, Ga) Se_2 thin-film solar cells beyond 20%. Prog Photovoltaics. 2011;19(7):894–7.

[61] Chirilă A, Reinhard P, Pianezzi F, Bloesch P, Uhl AR, Fella C, et al. Potassium-induced surface modification of Cu (In, Ga) Se_2 thin films for high-efficiency solar cells. Nat Mater. 2013;12(12):1107–11.
[62] Jackson P, Hariskos D, Wuerz R, Wischmann W, Powalla M. Compositional investigation of potassium doped Cu (In, Ga) Se_2 solar cells with efficiencies up to 20.8%. Phys Status Solidi RRL. 2014;8(3):219–22.
[63] Jackson P, Hariskos D, Wuerz R, Kiowski O, Bauer A, Friedlmeier TM, et al. Properties of Cu (In, Ga) Se_2 solar cells with new record efficiencies up to 21.7%. Phys. Status Solidi RRL. 2015;9(1):28–31.
[64] Kamada R, Yagioka T, Adachi S, Handa A, Tai KF, Kato T, et al. New world record Cu (In, Ga)(Se, $S)_2$ thin film solar cell efficiency beyond 22%. 2016 IEEE 43rd Photovoltaic Specialists Conference (PVSC). IEEE; 2016. p. 1287–91.
[65] Jackson P, Wuerz R, Hariskos D, Lotter E, Witte W, Powalla M. Effects of heavy alkali elements in Cu (In, Ga) Se2 solar cells with efficiencies up to 22.6%. Phys Status Solidi RRL. 2016;10(8):583–6.
[66] Gong J, Kong Y, Li J, Wang K, Wang X, Zhang Z, et al. Enhancing photocurrent of Cu (In, Ga) Se2 solar cells with actively controlled Ga grading in the absorber layer. Nano Energy. 2019;62:205–11.
[67] Koida T, Nishinaga J, Ueno Y, Higuchi H, Takahashi H, Iioka M, et al. Improved efficiency of Cu (In, Ga) Se2 mini-module via high-mobility In2O3: W, H transparent conducting oxide layer. Prog Photovoltaics. 2019;27(6):491–500.
[68] Nakamura M, Yamaguchi K, Kimoto Y, Yasaki Y, Kato T, Sugimoto H. Cd-free Cu (In, Ga)(Se, S) 2 thin-film solar cell with record efficiency of 23.35%. IEEE J Photovoltaics. 2019;9(6):1863–7.
[69] Kato T, Wu J-L, Hirai Y, Sugimoto H, Bermudez V. Record efficiency for thin-film polycrystalline solar cells up to 22.9% achieved by Cs-treated Cu (In, Ga)(Se, S) 2. IEEE J Photovoltaics. 2018;9(1):325–30.
[70] Youn S-M, Park M-J, Kim JH, Jeong C. Performance enhancement of CIGS thin-film solar cells with a functional-window NiO thin layer. J Alloy Compd. 2020;836:154803.
[71] Nishinaga J, Sugaya T. Crystalline characterisitics of epitaxial Cu (In, Ga) Se 2 layers on GaAs (001) substrates. 2020 47th IEEE Photovoltaic Specialists Conference (PVSC). IEEE; 2020. p. 2251–7.
[72] Siebentritt S, Avancini E, Bär M, Bombsch J, Bourgeois E, Buecheler S, et al. Heavy alkali treatment of Cu (In, Ga) Se2 solar cells: surface *versus* bulk effects. Adv Energy Mater. 2020;10(8):1903752.
[73] Nishinaga J, Ishizuka S. Effects of alkali-metal incorporation into epitaxial Cu (In, Ga) Se2 solar cells prepared by molecular beam epitaxy. Thin Solid Films. 2022;741:139034.
[74] Krause M, Nikolaeva A, Maiberg M, Jackson P, Hariskos D, Witte W, et al. Microscopic origins of performance losses in highly efficient Cu (In, Ga) Se2 thin-film solar cells. Nat Commun. 2020;11(1):4189.
[75] Carron R, Nishiwaki S, Yang S-C, Ochoa M, Sun X, Feurer T, et al. Heat-light soaking treatments for high-performance CIGS solar cells on flexible substrates; 2022. doi: 10.21203/rs.3.rs-2116168/v1.
[76] Nishinaga J, Togawa M, Miyahara M, Itabashi K, Okumura H, Imura M, et al. Annealing effects on Cu (In, Ga) Se2 solar cells irradiated by high-fluence proton beam. Jpn J Appl Phys. 2023;62:SK1014.
[77] Nishinaga J, Kamikawa Y, Sugaya T, Ishizuka S. Comparison of polycrystalline and epitaxial Cu (In, Ga) Se2 solar cells with conversion efficiencies of more than 21%. Sol Energy Mater Sol Cell. 2024;269:112791.
[78] Keller J, Kiselman K, Donzel-Gargand O, Martin NM, Babucci M, Lundberg O, et al. High-concentration silver alloying and steep back-contact gallium grading enabling copper indium gallium selenide solar cell with 23.6% efficiency. Nat Energy. 2024;9(4):467–78.
[79] Xu M, Yan S, Liang T, Jia J, Yuan S, Kou D, et al. 16.48% Efficient solution-processed CIGS solar cells with crystal growth and defects engineering enabled by Ag doping strategy. J Energy Chem. 2025;100:59–65.
[80] Eperon GE, Hörantner MT, Snaith HJ. Metal halide perovskite tandem and multiple-junction photovoltaics. Nat Rev Chem. 2017;1(12):0095.
[81] Ho-Baillie AW, Zheng J, Mahmud MA, Ma F-J, McKenzie DR, Green MA. Recent progress and future prospects of perovskite tandem solar cells. Appl Phys Rev. 2021;8(4):041307.
[82] Cheng Y, Ding L. Perovskite/Si tandem solar cells: Fundamentals, advances, challenges, and novel applications. SusMat. 2021;1(3):324–44.
[83] Geng C, Zhang K, Wang C, Wu CH, Jiang J, Long F, et al. Crystallization modulation and holistic passivation enables efficient two-terminal perovskite/CuIn (Ga) Se2 tandem solar cells. Nano-Micro Lett. 2025;17(1):8.
[84] Tian L, Bi E, Yavuz I, Deger C, Tian Y, Zhou J, et al. Divalent cation replacement strategy stabilizes wide-bandgap perovskite for Cu (In, Ga) Se2 tandem solar cells. Nat Photonics. 2025;19:479–85.
[85] Todorov T, Gershon T, Gunawan O, Lee YS, Sturdevant C, Chang LY, et al. Monolithic perovskite-CIGS tandem solar cells via in situ band gap engineering. Adv Energy Mater. 2015;5(23):1500799.
[86] Han Q, Hsieh Y-T, Meng L, Wu J-L, Sun P, Yao E-P, et al. High-performance perovskite/Cu (In, Ga) Se2 monolithic tandem solar cells. Science. 2018;361(6405):904–8.
[87] Jošt M, Bertram T, Koushik D, Marquez JA, Verheijen MA, Heinemann MD, et al. 21.6%-efficient monolithic perovskite/Cu (In, Ga) Se2 tandem solar cells with thin conformal hole transport layers for integration on rough bottom cell surfaces. ACS Energy Lett. 2019;4(2):583–90.
[88] Al-Ashouri A, Magomedov A, Roß M, Jošt M, Talaikis M, Chistiakova G, et al. Conformal monolayer contacts with lossless interfaces for perovskite single junction and monolithic tandem solar cells. Energy Environ Sci. 2019;12(11):3356–69.
[89] Kafedjiska I, Farias-Basulto GA, Reyes-Figueroa P, Bertram T, Al-Ashouri A, Kaufmann CA, et al. Integration of rough RTP absorbers into CIGS-perovskite monolithic tandems by NiO_x (: Cu) +SAM Hole-transporting Bi-layers. Sol Energy Mater Sol Cell. 2023;254:112248.
[90] Alvianto E, Wan G, Shi Z, Liang H, Wang X, Guo X, et al. Sustainable manufacturing of perovskite-CIGS tandem solar cells through lamination with metal-free transparent conductive adhesives. ACS Energy Lett. 2024;9(5):2057–64.
[91] Bailie CD, Christoforo MG, Mailoa JP, Bowring AR, Unger EL, Nguyen WH, et al. Semi-transparent perovskite solar cells for tandems with silicon and CIGS. Energy Environ Sci. 2015;8(3):956–63.
[92] Fu F, Feurer T, Jäger T, Avancini E, Bissig B, Yoon S, et al. Low-temperature-processed efficient semi-transparent planar perovskite solar cells for bifacial and tandem applications. Nat Commun. 2015;6(1):8932.

[93] Fu F, Feurer T, Weiss TP, Pisoni S, Avancini E, Andres C, et al. High-efficiency inverted semi-transparent planar perovskite solar cells in substrate configuration. Nat Energy. 2016;2(1):1–9.
[94] Guchhait A, Dewi HA, Leow SW, Wang H, Han G, Suhaimi FB, et al. Over 20% efficient CIGS–perovskite tandem solar cells. ACS Energy Lett. 2017;2(4):807–12.
[95] Shen H, Peng J, Jacobs D, Wu N, Gong J, Wu Y, et al. Mechanically-stacked perovskite/CIGS tandem solar cells with efficiency of 23.9% and reduced oxygen sensitivity. Energy Environ Sci. 2018;11(2):394–406.
[96] Nakamura M, Tada K, Kinoshita T, Bessho T, Nishiyama C, Takenaka I, et al. Perovskite/CIGS spectral splitting double junction solar cell with 28% power conversion efficiency. Iscience. 2020;23(12):101817.
[97] Feeney T, Hossain IM, Gharibzadeh S, Gota F, Singh R, Fassl P, et al. Four-terminal perovskite/copper indium gallium selenide tandem solar cells: unveiling the path to > 27% in power conversion efficiency. Sol RRL. 2022;6(12):2200662.
[98] Liu X, Zhang J, Tang L, Gong J, Li W, Ma Z, et al. Over 28% efficiency perovskite/Cu (InGa) Se 2 tandem solar cells: highly efficient sub-cells and their bandgap matching. Energy Environ Sci. 2023;16(11):5029–42.
[99] Tang L, Zeng L, Luo J, Wang W, Xue Z, Luo Z, et al. All-round passivation strategy yield flexible perovskite/CuInGaSe2 tandem solar cells with efficiency exceeding 26.5%. Adv Mater. 2024;36(28):2402480.
[100] Lee M, Park SJ, Hwang YJ, Jun Y, Min BK. Tandem architecture of perovskite and Cu (In, Ga)(S, Se) 2 created by solution processes for solar cells. Adv Opt Mater. 2016;4(12):2102–8.
[101] Kranz L, Abate A, Feurer T, Fu F, Avancini E, Löckinger J, et al. High-efficiency polycrystalline thin film tandem solar cells. J Phys Chem Lett. 2015;6(14):2676–81.
[102] Yang Y, Chen Q, Hsieh Y-T, Song T-B, Marco ND, Zhou H, et al. Multilayer transparent top electrode for solution processed perovskite/Cu (In, Ga)(Se, S) 2 four terminal tandem solar cells. ACS Nano. 2015;9(7):7714–21.
[103] Li Z, Zhao Y, Wang X, Sun Y, Zhao Z, Li Y, et al. Cost analysis of perovskite tandem photovoltaics. Joule. 2018;2(8):1559–72.
[104] Wang L, Zai H, Duan Y, Liu G, Niu X, Ma Y, et al. Cost analysis of perovskite/Cu (In, Ga) Se2 tandem photovoltaic with module replacement. ACS Energy Lett. 2022;7(6):1920–5.
[105] Ahangharnejhad RH, Phillips AB, Song Z, Celik I, Ghimire K, Koirala P, et al. Impact of lifetime on the levelized cost of electricity from perovskite single junction and tandem solar cells. Sustain Energy & Fuels. 2022;6(11):2718–26.
[106] Celik I, Philips AB, Song Z, Yan Y, Ellingson RJ, Heben MJ, et al. Energy payback time (EPBT) and energy return on energy invested (EROI) of perovskite tandem photovoltaic solar cells. IEEE J Photovoltaics. 2017;8(1):305–9.
[107] Celik I, Phillips AB, Song Z, Yan Y, Ellingson RJ, Heben MJ, et al. Environmental analysis of perovskites and other relevant solar cell technologies in a tandem configuration. Energy Environ Sci. 2017;10(9):1874–84.
[108] Celik I, Song Z, Cimaroli AJ, Yan Y, Heben MJ, Apul D. Life Cycle Assessment (LCA) of perovskite PV cells projected from lab to fab. Sol Energy Mater Sol Cell. 2016;156:157–69.
[109] Boukortt NEI, Patanè S, Loureiro AG, AlAmri AM, Abdulraheem YM, Lenka TR, et al. Electrical and optical investigation of 2T–perovskite/u-CIGS tandem solar cells with~ 30% efficiency. IEEE Trans ElectrDevices. 2022;69(7):3798–806.
[110] Zhao P, Feng L, Lin Z, Wang J, Su J, Hu Z, et al. Theoretical analysis of two-terminal and four-terminal perovskite/copper indium gallium selenide tandem solar cells. Sol RRL. 2019;3(11):1900303.
[111] Jung S-K, Park N-G, Lee J-W. Light management in perovskite solar cells. Mater Today Energy. 2023;37:101401.
[112] Oliveira AJ, Teixeira JP, Ramos D, Fernandes PA, Salomé PM. Exploiting the optical limits of thin-film solar cells: a review on light management strategies in Cu (In, Ga) Se_2. Adv Photonics Res. 2022;3(6):2100190.
[113] Shafian S, Mohd Salehin FN, Lee S, Ismail A, Mohamed Shuhidan S, Xie L, et al. Development of organic semiconductor materials for organic solar cells via the integration of computational quantum chemistry and AI-powered machine learning. ACS Appl Energy Mater. 2025;8(2):699–722.
[114] Mao L, Xiang C. A comprehensive review of machine learning applications in perovskite solar cells: materials discovery, device performance, process optimization and systems integration. Mater Today Energy. 2024;47:101742.
[115] Kim Y, Son J, Shafian S, Kim K, Hyun JK. Semitransparent blue, green, and red organic solar cells using color filtering electrodes. Adv Opt Mater. 2018;6(13):1800051.
[116] Shafian S, Son J, Kim Y, Hyun JK, Kim K. Active-material-independent color-tunable semitransparent organic solar cells. ACS Appl Mater & Interfaces. 2019;11(21):18887–95.
[117] Kim BY, Shafian S, Kim K. High-performance semitransparent color organic photodiodes enabled by integrating fabry–perot and solution-processed distributed bragg reflectors. Adv Mater Interfaces. 2023;10(31):2300421.
[118] Shafian S, Eun Lee G, Yu H, Jeong J-H, Kim K. High-efficiency Vivid color CIGS solar cell employing nondestructive structural coloration. Sol RRL. 2022;6(4):2100965.
[119] Shafian S, Kim K. Panchromatically responsive organic photodiodes utilizing a noninvasive narrowband color electrode. ACS Appl Mater Interfaces. 2020;12(47):53012–20.
[120] You Y-J, Saeed MA, Shafian S, Kim J, Kim SH, Kim SH, et al. Energy recycling under ambient illumination for internet-of-things using metal/oxide/metal-based colorful organic photovoltaics. Nanotechnology. 2021;32(46):465401.
[121] Park S, Shafian S, Lee J, Jo S, Jeon S, Lee S, et al. High-efficiency structural coloration enabled by defect-free block copolymer self-assembly for a solar cell distributed bragg reflector. Adv Opt Mater. 2023;11(24):2301357.